Estimation of Stiffness Maps in Deforming Cells Through Optical Flow With Bounded Curvature

Yekta Kesenci, Aleix Boquet-Pujadas, *Member, IEEE*, Michael Unser, *Life Fellow, IEEE*, and Jean-Christophe Olivo-Marin, *Fellow, IEEE*

***Abstract*— The stiffness of cells and of their nuclei is a biomarker of several pathological conditions. Current measurement methods rely on invasive physical probes that yield one or two stiffness values for the whole cell. However, the internal distribution of cells is heterogeneous. We propose a framework to estimate maps of intracellular and intranuclear stiffness inside deforming cells from fluorescent image sequences. Our scheme requires the resolution of two inverse problems. First, we use a novel optical-flow method that penalizes the nuclear norm of the Hessian to favor deformations that are continuous and piecewise linear, which we show to be compatible with elastic models. We then invert these deformations for the relative intracellular stiffness using a novel system of elliptic PDEs. Our method operates in quasi-static conditions and can still provide relative maps even in the absence of knowledge about the boundary conditions. We compare the accuracy of both methods to the state of the art on simulated data. The application of our method to real data of different cell strains allows us to distinguish different regions inside their nuclei.**

***Index Terms*— Mechanobiology, elastography, nucleus, nuclear norm.**

I. Introduction

CELLULAR stiffness has been proposed as a biomarker of diseases such as cancer or laminopathies [1], [2]. It also plays a key role in cell migration [3]. The stiffness of the cell nucleus is of special interest in these contexts [4]. The nucleus houses the genome in the form of chromatin. In particular, nuclear DNA is packaged into light (euchromatin) or dense (heterochromatin) structures. The organization into these structures regulates cellular functions as fundamental as gene expression [5] and DNA replication [6]. Whereas the disorganization thereof has been linked to pathologies such as muscular dystrophy [7], progeria [8], and cancer [4]. Since the proportion of euchromatin to heterochromatin has an impact on the stiffness of the nucleus [9], biologists often use Young's modulus as a biomarker of disease [10]. Other structures including the lamina, which envelops the nucleus internally for mechanical support, influence stiffness too.

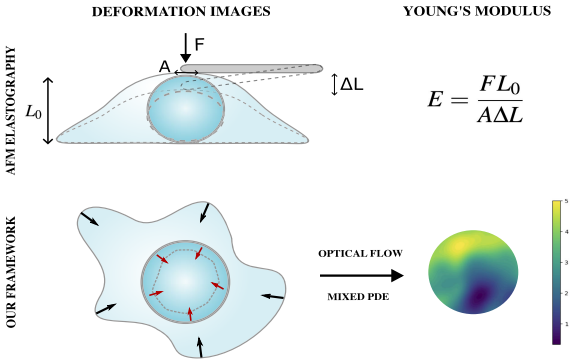

Fig. 1. Typical methods in biology recover one single value E for the nuclear stiffness with invasive methods. For example, by pressing the cell with an atomic-force microscope (AFM) and measuring ΔL. Our framework (novel optical flow and elastography) recovers the distribution $E(r)$ of intranuclear stiffness while the cell (black arrows) and its nucleus (red arrows) move freely.

In medical elastography, ultrasound imaging is used to probe the stiffness of tissues. But this is not easily applicable to biological settings [11]. To measure the Young's modulus of the cell or its nucleus, researchers rely instead on the application of dynamic or quasi-static loads [12]. For example, by aspiration with a micropipette, by compression between plates, or by poking with a small cantilever in what is known as atomic force microscopy (AFM) [12]. These techniques can damage the cell and require it to be both physically accessible and immobile. Moreover, they use simplified formulas to turn the length of the deformation into a single figure of merit—the average elastic modulus—for the whole nucleus (Figure 1), or for the whole cell [13]. This makes it difficult to isolate the actual source (euchromatin, lamin, etc.) of any differences in stiffness.

We propose to leverage the deformation of cells to estimate a heterogeneous map of their relative internal stiffness $E(\mathbf{r})$.

Received 26 July 2024; revised 7 October 2024; accepted 4 November 2024. Date of publication 8 November 2024; date of current version 14 March 2025. This work was supported in part by the TOXONUC Project under Grant ANR-19-CE13-0034-02, in part by the Labex IBEID under Grant ANR-10-LABX-62-IBEID, in part by France-BioImaging Infrastructure under Grant ANR-10-INBS-04, in part by the Institut Carnot Pasteur Microbes et Santé under Grant ANR-16-CARN-0023-01, and in part by the Swiss National Science Foundation under the Sinergia Grant CRSII5_198569. *(Yekta Kesenci and Aleix Boquet-Pujadas contributed equally to this work.) (Corresponding authors: Aleix Boquet-Pujadas; Jean-Christophe Olivo-Marin.)*

Yekta Kesenci and Jean-Christophe Olivo-Marin are with CNRS UMR 3691, BioImage Analysis Unit, Institut Pasteur, 75015 Paris, France, and also with Université Paris Cité, 75006 Paris, France (e-mail: yekta.kesenci@pasteur.fr; jcolivo@pasteur.fr).

Aleix Boquet-Pujadas and Michael Unser are with the Biomedical Imaging Group, École Polytechnique Fédérale de Lausanne (EPFL), 1015 Lausanne, Switzerland (e-mail: aleix.boquetipujadas@epfl.ch; michael.unser@epfl.ch).

Digital Object Identifier 10.1109/TMI.2024.3494050

1558-254X © 2024 IEEE. Personal use is permitted, but republication/redistribution requires IEEE permission.
See https://www.ieee.org/publications/rights/index.html for more information.

Authorized licensed use limited to: EPFL LAUSANNE. Downloaded on March 24,2025 at 15:29:48 UTC from IEEE Xplore. Restrictions apply.

This is applicable to the natural deformations that cells undergo when moving freely through the obstacles in their microenvironment *in vivo*, as well as to *in vitro* experiments where the cell is intentionally squeezed (Figure 1). We consider cells (or nuclei) that are labelled with a fluorescent marker. The idea is to estimate the intracellular (or intranuclear) displacements $\mathbf{u}(\mathbf{r})$ from image sequences using an optical flow (OF) technique, and to then invert them using a continuum mechanics model to obtain the relative stiffness map $E(\mathbf{r})$. This comes with several challenges.

A first challenge is the relatively high compressibility of the cell and its nucleus [14]. This precludes methods that exploit incompressibility [15], thereby making the stiffness-inversion process potentially prohibitive for the analysis of the large datasets (e.g., extensive statistical populations, multiple conditions, 3D acquisitions) typical of biological experiments [16]. A second challenge is that most stiffness-inversion methods require knowledge of the traction force everywhere on the boundary [17], [18]. Recovering this traction is incompatible with our experiments because it requires complex experimental setups that measure a single spatial point at a time in immobile cells. An alternative way to obtain the traction is to differentiate the boundary displacements. However, this greatly amplifies experimental errors, and thus may only be tolerated by using costly constrained methods [19], or by reducing the high-dimensional stiffness map to two variables as done for the nucleus of beating cells [20]. This brings us to the third challenge: stiffness-inversion methods are inherently sensitive to noise in the displacement input. This is because the relevant quantities are the spatial derivatives of the displacement (the strain). We argue that the inversion would be better posed if the regularity properties of the displacements were more compatible with those required by the elasticity equations. While our framework is applicable to the estimation of intracellular stiffness in general, we will focus on the nucleus for concreteness.

A. Contributions

The main contribution of this work is a method to estimate the stiffness map in the nuclei of deforming cells. This is done computationally from a pair of images taken before and after the deformation.

Three additional contributions were necessary to develop this method:

i. The formulation of the problem in a framework that matches our experimental setup (Section II). We study the regularity conditions in light of the biological configuration of the nucleus.
ii. A refinement of OF that favors displacements that are continuous and piecewise linear, and thus more compatible with the elasticity equations (Section III-A). The regularization is based on the nuclear norm of the Hessian of the displacement field, which promotes small curvatures in a sparse manner.
iii. The development of a novel method to invert the displacements for the relative[1] stiffness map in a way that is efficient for application to large datasets (Section III-B). This is based on a modified system of elliptic partial differential equations (PDE) of the relative stiffness. It accounts for the compressibility of the nucleus and does not require knowledge of the traction boundary conditions to yield relative values.

We individually compare our methods proposed in (i) and (ii) to the state of the art using simulated data. Experiments with real data show that our method can differentiate the stiffness of different components inside the nucleus (Section IV).

We had already introduced point (ii) in our conference paper [22]. In the current paper, however, we expand (ii) in terms of the justification (function spaces and solutions) and provide new analyses (e.g., noise-sensitivity, large deformations, slicing), and a 3D example. We also introduce (i), (iii).

B. Current Methods to Estimate Intracellular Stiffness

Our main application for Contributions (i)-(iii) is the estimation of relative-stiffness maps inside cells. Here, we provide a small review of techniques to measure cellular and nuclear stiffness. We have divided them into three categories for simplicity—a more thorough review can be found in [12].

Probing techniques deform the nucleus with some probe. They derive the stiffness by relating the force applied by the probe to a measure of the deformation of the cell. In AFM [23], one pokes the cell with a cantilever and measures the axial squeezing of the nucleus (Figure 1). In micropipette aspiration [24], one applies negative pressure and measures the elongation of the nucleus. And, with optical tweezers [25], one pulls on a bead that is attached to the cell and measures the displacement of the former. Other examples are plate compressions [26] and magnetic tweezers [27]. All these techniques typically let the strain be summarized by a single axial value and use Hooke's law to derive a single value of stiffness. This value is quantitative only when the force applied has been calibrated in advance.

Microenvironment techniques alter the microenvironment of the cell to indirectly measure its properties. In general, these techniques do not yield a value for the stiffness but a value that is merely correlated thereto, often because of the intractability of the underlying model. The resulting values are still quantitative and, thus, are useful to rank (compare) different cell populations. The most representative example is, perhaps, the use of microfluidic devices to hinder the migration of cells [28], [29]. In these techniques, the measurable values are either the time it takes for the cell to go through the obstacle, or the maximal elongation of the nucleus. Other examples are the the use of shear flows [30] and the application of osmotic shocks, which result in volume changes [31].

Microscopy-based techniques enable measurements in cells that are moving freely through more physiological environments. For example, Brillouin microscopy relies on measures of the scattering of light to infer elasticity maps of biological tissues [32], even if there is an ongoing debate about what exactly is being measured [33]. While Brillouin microscopy requires somewhat specialized equipment, the work in [20] uses images from a standard epifluorescence microscope to

[1]The relative (i.e., "up to a constant", or unit-less) maps of stiffness can be made specific if the traction applied is known [21], or if the stiffness itself can be inferred at any point within the map.

Authorized licensed use limited to: EPFL LAUSANNE. Downloaded on March 24,2025 at 15:29:48 UTC from IEEE Xplore. Restrictions apply.

infer the relative stiffness between two pre-segmented intracellular regions. A last example is the estimation of the cell's local rheology through the diffusion scale of particle tracers [34].

The method resulting from bringing together Contributions (i)-(iii) could be considered a microscopy-based technique because it relies on fluorescence-microscopy images alone and does not require one to manipulate the cell. Moreover, our method does not yield single estimates, but entire stiffness maps. These maps are, in principle, of *relative* stiffness. However, they could be made *specific* by combining them with a probing technique (see Section V) or with a calibrated microenvironment.

II. Problem Analysis and State of the Art

In this Section, we present a continuum-mechanics model of the cell and look at the regularity properties of both the deformation and stiffness variables. We then go through state-of-the-art methods in OF and elastography to measure deformation and stiffness, respectively, and assess their pros and cons in this context. The resulting observations motivate the development of our own approaches thereof, which are formulated in Section III.

A. Elasticity of the Nucleus and Regularity Requirements

Under small deformations and quasi-static loads such as those involved in our proposed experiments of deforming cells (Figure 1), the nucleus behaves like a linearly elastic isotropic material [35]. Specifically, the displacements $\mathbf{u} : \Omega \to \mathbb{R}^d$ inside the nuclear domain $\Omega \subset \mathbb{R}^d$, $d \in \{2, 3\}$, behave according to

$$\begin{cases} \nabla \cdot \varsigma = 0, & \text{in } \Omega, \\ \mathbf{u} = \mathbf{g}, & \text{on } \Gamma_{\mathbf{g}}, \\ \varsigma \cdot \mathbf{n} = \mathbf{T}, & \text{on } \Gamma_{\mathbf{T}}, \end{cases} \tag{1}$$

where the stress $\varsigma : \Omega \to \mathbb{R}^d \times \mathbb{R}^d$ and the strain $\varepsilon : \Omega \to \mathbb{R}^d \times \mathbb{R}^d$ are defined as

$$\varsigma(\mathbf{u}) = \lambda \operatorname{Tr}(\varepsilon(\mathbf{u}))\mathbb{1} + 2\mu\varepsilon(\mathbf{u}), \tag{2}$$

$$\varepsilon(\mathbf{u}) = \frac{1}{2}(\nabla\mathbf{u} + \nabla\mathbf{u}^{\mathrm{T}}). \tag{3}$$

Here, $\mathbf{g} : \Omega \to \mathbb{R}^d$ and $\mathbf{T} : \Omega \to \mathbb{R}^d$ are the displacements and the applied traction on the boundary, which is split into $\partial\Omega = \Gamma_g \cup \Gamma_T$ and has $\mathbf{n}(\mathbf{r}) \in S^1$ as its normal vector [36].

The Lamé parameters $\lambda, \mu \in \mathbb{R}_{>0}$ are related to the stiffness E through the relations $\lambda = E\nu/(1+\nu)(1-2\nu)$ and $\mu = E/2(1+\nu)$, where ν is Poisson's ratio. In this work, we consider that the stiffness varies across the domain, $E(\mathbf{r})$, $\mathbf{r} \in \Omega$. Our aim is to reconstruct $E(\mathbf{r})$ from images of a deforming nucleus by first estimating a displacement field $\mathbf{u}(\mathbf{r})$. We argue that the reconstruction will be better when the estimated displacement matches that of an elastic material.

To this end, let us comment on the regularity of the solutions to the linear-elasticity equations. The nucleus is made up of well-delimited structures (lamin, euchromatin, heterochromatin…) of different stiffness. We interpret that this forms a piecewise-constant map of stiffness (e.g., Figure 2). In Appendix A, we show that the axial displacements upon an uniaxial stretching of such a configuration of the material are piecewise linear.

We can also study the solutions from the perspective of functional analysis. Consider that $\partial\Omega \in \mathscr{C}^\infty$. The smoothness of the boundary can be justified by the stiff lamina meshwork that scaffolds the nuclear envelope from the inside [37]. Consider also that $E \in L^1(\Omega, \mathbb{R})$ or $E \in H^2(\Omega, \mathbb{R})$. This is in line with the fractal-like configuration of chromatin [38], which can become smoother upon observation through the microscope. Then, considering pure Dirichlet ($\Gamma_{\mathbf{T}} = \emptyset$) or pure Neumann ($\Gamma_{\mathbf{g}} = \emptyset$) boundary conditions, (1) admits a strong solution $\mathbf{u} \in H^2(\Omega, \mathbb{R}^d)$ that is unique (up to the additive term $\mathbf{a} + \mathbf{bx}$ with $\mathbf{b}$ skew symmetric, in the Neumann case) [39]. In particular, this implies that the displacement must be continuous.

We design an optical-flow method that promotes solutions close to the solutions of (1) by studying the solution space and promoting displacements that are close to piecewise linear.

B. Standard Optical-Flow Methods

Let $I : \Omega_I \times T \to \mathbb{R}_{\geq 0}$ be the intensity of an image sequence over time, $T \subset \mathbb{R}$, on a spatial domain $\Omega_I \supset \Omega$. OF methods estimate the apparent displacement field $\tilde{\mathbf{u}}$ from the images by solving variational problems similar to

$$\tilde{\mathbf{u}} \in \arg\min_{\mathbf{u}} \left|\left|\frac{\partial I}{\partial t} + \mathbf{u} \cdot \nabla I\right|\right|^p_{\Omega_I, p} + \alpha R(\mathbf{u}), \tag{4}$$

In (4), the minimization of the data term (left) enforces the conservation of the intensity across images [40] according to the p norm over the domain Ω_I. The regularization term $R(\mathbf{u})$ (right) mitigates the ill-posedness of the previous assumption with *a priori* information about $\mathbf{u}(\mathbf{r})$. The weighting parameter $\alpha \in \mathbb{R}_{>0}$ balances the data and regularization terms. OF has been shown to outperform other particle-image velocimetry methods in biological samples [41], [42].

Most OF methods are engineered to address the problems of estimating 3D real-world motion from 2D images. Three such problems are image occlusion [43], illumination changes [44], and the discontinuities across the boundaries of moving objects [45].

The first two problems challenge the intensity conservation enforced by the data term in (4). This has been tackled with robust penalty functions [46], local layering [47], and extracting abstract features with convolutional neural networks [48]. In our case of fluorescence microscopy, brightness constancy is an adequate assumption because the fluorophores emit light in proportion to their concentration. Photobleaching may reduce the intensity over long acquisitions, but in a way that is roughly homogeneous and that can be addressed by normalizing over time. In addition, confocal microscopy in transparent samples such as cells precludes occlusions.

The third problem—discontinuities—is typically addressed through the regularization term $R(\mathbf{u})$. To ease the optimization procedure, most methods enforce their regularization functional to be lower semi-continuous, and convex. Typical

Authorized licensed use limited to: EPFL LAUSANNE. Downloaded on March 24,2025 at 15:29:48 UTC from IEEE Xplore. Restrictions apply.

optical-flow methods regularize the Jacobian of the displacement. For instance, $R(\mathbf{u}) = \int_{\Omega_I} |\nabla \mathbf{u}|^s$, with $s \geq 1$ [49]. For $s = 2$ one recovers the classical Horn-Schunck formulation, whereas $s = 1$ corresponds to one possible formulation of the widespread total variation (TV) regularization. TV is better approached through its dual formulation. This constrains the solution to the space of bounded variations $BV^{(1)}(\Omega_I, \mathbb{R}^d)$, which contains $W^{1,1}(\Omega_I, \mathbb{R}^d)$ but also allows for jump discontinuities across hypersurfaces [50], which are incompatible with elasticity. While suitable for the rigid motions predominant in every-day images, TV regularization is less adequate in our case. First, the displacements inside the nuclear domain are theoretically restricted to the smaller space $H^2(\Omega, \mathbb{R}^d)$. But, most importantly, TV regularization is known to promote piecewise-constant solutions, often giving rise to staircasing effects [51]. To increase the accuracy at the border of objects, some TV methods introduce additional elements such as soft segmentation cues [52] or dense correspondences matching [53].

TV artifacts are acceptable in most image-processing applications, but become a bigger drawback in elasticity reconstruction. This is because the strain tensor requires the differentiation of the displacements. More generally, TV regularizers favor piecewise-constant displacements instead of continuous and piecewise linear.

C. Standard Elastography Methods

Elastography methods aim at the reconstruction of stiffness maps $E(\mathbf{r})$ from displacement fields $\mathbf{u}(\mathbf{r})$ such as those recovered by OF. They do so via elasticity models such as (1). Quasi-static elastography methods have been developed for medical imaging and can take two forms: direct reconstruction methods, and indirect reconstruction methods [19], [54]. In either case, the algorithms require knowledge of the traction forces $\mathbf{T}$. If the stiffness is assumed homogeneous at the boundary, one can recover $\mathbf{T}$ from the displacements $\mathbf{u}_{|\partial\Omega}$ at the boundary, but at the price of differentiation.

On one hand, direct methods are fast but vulnerable to noise because they invert the matrix of the system directly. Let $\hat{\mathbf{u}}$ be the discrete coefficients of $\mathbf{u}$ in some basis, for example of finite elements [17]. Then, (1) can be discretized into the sparse linear system of equations $\mathbf{K}\hat{\mathbf{u}} = \mathbf{t}$ with $\mathbf{K}$ the stiffness matrix—which depends on the basis used for discretization and on E—and $\mathbf{t}$ the discretization of $\mathbf{T}$. This system can be rearranged into the alternative system $\mathbf{B}\hat{\mathbf{e}} = \mathbf{t}$ to instead bring out the coefficients $\hat{\mathbf{e}}$ of the stiffness E. Here, $\mathbf{B}$ is a matrix that depends on the basis and on $\hat{\mathbf{u}}$.

Thanks to the sparsity of $\mathbf{B}$, a direct inversion scheme can recover the stiffness $\hat{\mathbf{e}}$ in a computationally efficient way. Direct methods are very accurate in the axial direction of the deformation. However they are very sensitive to noise, and usually fail entirely when the traction at the boundary is unknown. These limitations have only been overcome for incompressible materials [55]. This is because the lateral displacements, which are the most sensitive to noise, are informed by the axial displacements because of the field being divergence-free. Unfortunately, biological material is compressible.

On the other hand, indirect reconstruction methods use the computed displacement field $\tilde{\mathbf{u}}_{|\Omega}$ to feed a PDE-constrained optimization framework of the form

$$\begin{aligned} &\arg\min_{\mathbf{u},E} \; J(\mathbf{u}, E) = ||\mathbf{u} - \tilde{\mathbf{u}}_{|\Omega}||^2_{\Omega,2} + \beta G(E) \\ &\text{subject to Eq. (1)}, \end{aligned} \tag{5}$$

where $\beta \in \mathbb{R}_{>0}$ is the weighting parameter, and $G(E)$ regularizes the stiffness E; for example, $G(E) = ||E||^2_{\Omega,2}$ in [18]. In other works, the optical-flow term is included directly into the PDE-constrained framework [56], [57]. In practice, indirect methods are robust to noise due to the regularization term. It is unclear how exactly the space where the displacements belong to affects the accuracy of the reconstruction, but, at least, one expects that more realistic and continuous displacements should bear better reconstructions. Usually, problem (5) admits an unconstrained formulation that can be solved with a quasi-Newton gradient-descent algorithm [18]. However, even if the gradient can be computed with an adjoint-based approach [58], indirect methods are often too slow for application to large biological datasets.

III. Proposed Framework

In light of the challenges and requirements outlined in Section II, we now propose our own OF and elastography methods.

A. Proposed Optical-Flow Method (HTV)

We refer to our proposed OF method as Hessian-based total variation (HTV).

1) Motivation for the Regularization: To promote solutions to the OF problem that are closer to those of the elasticity equations, we propose to regularize the Hessian of the displacements. We do so through the mixed nuclear-$\mathscr{M}$ norm $||\mathscr{H}\{\mathbf{u}_i\}||_{*,\mathscr{M}} = \big|\big|\big|\mathscr{H}\{\mathbf{u}_i\}\big|\big|_*(\mathbf{x})\big|\big|_{\mathscr{M}}$, where $\mathscr{H}\{\cdot\}$ is the generalized Hessian operator, and $\mathscr{M}$ denotes the space of finite Radon measures equipped with the total-variation norm (in the sense of measures) [59]. If $\mathbf{u}$ is twice differentiable, this is equivalent to

$$||\mathscr{H}\{\mathbf{u}_i\}||_{*,\mathscr{M}} = ||\mathscr{H}\{\mathbf{u}_i\}||_{*,1} = \int_\Omega \sum_{k=1}^{d} |\sigma_k\{\mathscr{H}\{\mathbf{u}_i\}(\mathbf{x})\}| \mathrm{d}\mathbf{x}, \tag{6}$$

where $\sigma_k\{\cdot\}$ maps to the k-th singular value of the matrix, and $\mathscr{H}$ reduces to the classical Hessian.

This choice of norm will promote continuous and close-to-piecewise-linear solutions. This is precisely what we expect from some of our elastic problems, as per the reasoning in Appendix A and Section II-A. These solutions are promoted because the regularization enforces a small principal curvature (i.e., small singular values of the Hessian) over the entire displacement field in a sparse way. (Note that the curvature of piecewise-linear functions is zero everywhere except at the "knots".)

Our regularization strategy also acts as a surrogate for the promotion of low-rank matrices.

Authorized licensed use limited to: EPFL LAUSANNE. Downloaded on March 24,2025 at 15:29:48 UTC from IEEE Xplore. Restrictions apply.

In addition, the nuclear norm is invariant to rotation, translation, and scaling, which is helpful in the reconstruction of a physical signal such as the displacement. It is also computationally efficient: since the Hessian is symmetric, its nuclear norm can be expressed analytically in terms of the eigenvalues for $d \leq 4$.

We regularize each component of the displacement separately for two reasons. First, the piecewise linearity of elastic solutions often has a distinct direction that aligns with potential tractions (see Appendix A). And, second, considering both components together would require the nuclear norm of a third order tensor, which is not invariant to rotation and is NP-hard to compute [60], [61].

2) Formulation of the Inverse Problem: The novel variational problem we propose to solve for computing OF is then

$$\tilde{\mathbf{u}} \in \underset{\substack{\mathbf{u}=(\mathbf{u}_1,\mathbf{u}_2)\\ \in \mathrm{BV}^{(2)}(\Omega_I,\mathbb{R}^2)}}{\operatorname{argmin}} \left(\left|\left| \frac{\partial I}{\partial t} + \mathbf{u}\cdot\nabla I \right|\right|^p_{\Omega_I,p} + \alpha_1 ||\mathscr{H}\{\mathbf{u}_1\}||_{*,\mathscr{M}} + \alpha_2 ||\mathscr{H}\{\mathbf{u}_2\}||_{*,\mathscr{M}} \right), \tag{7}$$

where we focus on $d = 2$ and $\alpha_1, \alpha_2 \in \mathbb{R}_{\geq 0}$ are regularization hyperparameters (see Appendix C).

We have explored problem (7) with $p \in \{1, 2\}$. Overall, we obtained better OF results with the 1 norm and, therefore, it is the one we chose for our OF experiments, albeit the 2 norm was sometimes better in combination with elastography. Problem (7) is well defined over the space $BV^{(2)}(\Omega_I, \mathbb{R}^2)$, where the regularization term is convex and lower semi-continuous [62], [63].

Compared to TV, this is a smaller space containing $H^2(\Omega_I, \mathbb{R}^2)$, and thus closer to the space where the solutions to the linear-elasticity equation (1) belong to (while also allowing for jumps). The solutions are also required to be continuous. We observe that they are close to piecewise linear too.

As is common in OF techniques [64], we adopt a multiresolution approach to deal with large displacements.

3) Algorithm: The problem in (7) is convex because all terms therein are convex. We solve the (discrete) pixel version of (7) with $p = 1$ using the alternating direction method of multipliers (ADMM). The proximal operator of the OF term is a soft-thresholding operator. Since the regularization functional is separable, we can consider the proximal operator of each component separately. Neither admits a closed-form solution. Instead, we approximate the proximal operator of the nuclear norm of the Hessian of each component by solving a primal-dual optimization problem with a Nesterov approach [65] (Figure S1). In the case of $p = 2$, the OF term is differentiable. Therefore, we have used accelerated proximal-gradient descent (monotone FISTA [66]) with a step size adjusted according to the Lipschitz bound derived in Appendix B.

We compute the image derivatives according to [40]. We do this at each step of the multiresolution scheme: we then project the solution onto a finer scale and warp the image [64].

TABLE I

RMSE OF THE RECONSTRUCTIONS OF THE DISPLACEMENT FIELD FOR VARYING STRETCHING CONDITIONS (TRACTIONS, RATIOS, MODULI, AND NUMBERS OF INCLUSIONS). THE DIMENSION OF THE IMAGES IS (100 × 100) PIXELS. THE PSNR IS SET TO 30 dB

OF	RMSE $\mathbf{u}$ $(\cdot 10^{-2})$ [px]			
	T	ν	E	Nb. inc.
HTV	**3.63 ±0.20**	**3.82 ±0.42**	**3.79 ±0.41**	**3.76 ±0.37**
TV	6.05 ±0.42	6.45 ±0.69	6.60 ±0.64	6.71 ±0.62
HS	5.53 ±0.79	7.05 ±1.86	7.00 ±1.52	6.82 ±1.42
LDOF	7.03 ±1.80	20.04 ±21.72	16.14 ±18.58	14.82 ±16.83
ILK	4.63 ±0.80	6.20 ±2.94	6.23 ±2.42	6.25 ±2.18

B. Proposed Elastography Method (Mixed-PDE)

To improve the estimation of the stiffness map, we propose to modify the system of elastic PDEs. To this end, we first substitute the constitutive equation (2) into the momentum equation (1), and rearrange the terms into the first-order (for E) system of equations

$$\begin{bmatrix} l\varepsilon_{11} + (l-m)\varepsilon_{22} & m\varepsilon_{12} \\ m\varepsilon_{21} & (l-m)\varepsilon_{11} + l\varepsilon_{22} \end{bmatrix} \begin{bmatrix} \partial_x \ln(E) \\ \partial_y \ln(E) \end{bmatrix} = -\begin{bmatrix} \partial_x(l\varepsilon_{11} + (l-m)\varepsilon_{22}) + \partial_y(m\varepsilon_{12}) \\ \partial_x(m\varepsilon_{21}) + \partial_y((l-m)\varepsilon_{11} + l\varepsilon_{22}) \end{bmatrix}, \tag{8}$$

where $l = (1-\nu)/((1+\nu)(1-2\nu))$ and $m = 1/(1+\nu)$. This formulation extends the work of [67] for incompressible tissues to our compressible biological material. Other works on elasticity inversion have used second-order PDEs instead [68], [69]. All the PDEs mentioned are hyperbolic and can be solved with the method of characteristics.

If one considers that E is known over the boundary, one can infer from [54] that (8) has a unique solution. This is applicable to our experimental setup because the boundary of the nucleus is covered consistently by the lamina, and because our interest lies in relative stiffness only. However, the inversion of the hyperbolic PDEs is sensitive to noise. This is a drawback of the other direct methods too.

To better condition the problem, we consider adding a (small) stabilizing term to make (8) elliptic. Let us write (8) as $\mathscr{A}\nabla\ln(E) = \mathscr{F}$ with $\mathscr{A}(\mathbf{r}), \mathscr{F}(\mathbf{r}) \in \mathbb{R}^2$, which is well-defined for $\mathbf{u} \in H^2(\Omega, \mathbb{R}^2)$. Instead of (8), we propose to use

$$\mathscr{A}\nabla\ln(E) + \mathscr{B} = \mathscr{F}, \tag{9}$$

$$\mathscr{B} = \Delta\{\ln(E)\}(\gamma_1, \gamma_2), \tag{10}$$

where $\Delta\{\cdot\}$ is the Laplacian operator, and $\gamma_1, \gamma_2 \in \mathbb{R}_{\geq 0}$ are constants. The addition of stabilization terms such as $\mathscr{B}$ is common in hard-to-solve PDEs; here we use $\mathscr{B}$ as an implicit regularization term. In a way, the ellipticity of (9) better represents the static behavior of the stiffness distribution. From the perspective of physics, $\mathscr{B}$ adds diffusion to the PDE whereas, from that of signal-processing, it acts similarly to a lowpass filter and counteracts noise.

Finally, to deal with the potentially complicated geometry of the nucleus, we rewrite (9) into a variational form that is amenable to the finite element method (FEM). Let us introduce the new variable $\sigma = \nabla\ln(E)$. We multiply this system with test functions $\tau = (\tau_1, \tau_2)$ and v. By integrating over

Authorized licensed use limited to: EPFL LAUSANNE. Downloaded on March 24,2025 at 15:29:48 UTC from IEEE Xplore. Restrictions apply.

Ω and applying Green's identity, we get the following weak formulation:

$$\begin{cases} \int_\Omega \mathscr{A}\sigma \cdot \tau + (\gamma_1, \gamma_2) \cdot \int_\Omega \nabla(\tau_1, \tau_2)\sigma = \int_\Omega \mathscr{F} \cdot \tau \,, \\ \int_\Omega \sigma \cdot v = \int_\Omega \nabla \ln(E) \cdot v \,. \end{cases} \tag{11}$$

Equation (11) is elliptic and can be used for arbitrary domains of compressible material even when the traction at the boundary is not known.

1) Algorithm: We solve (11) numerically with the FEM. After meshing domain Ω, we discretize the functions in (8) à la Galerkin [70] using second-order piecewise polynomials. This results in a linear system. The matrix resulting from assembling (11) is sparse, but indefinite and non-symmetric. Therefore, we resort to a Krylov method [71], namely the generalized minimal residual method (GMRES) preconditioned with incomplete LU factorization. The framework scales linearly with the dimension of the discretization. We impose that E takes a reference value at a certain subset of the domain to obtain a relative stiffness. The stiffness is recovered by exponentiating the solution of (11). We have noticed that we get better reconstructions upon running this algorithm twice (a first time with a positive pair (γ_1, γ_2) of regularization parameters and a second time with their negative counterparts) and averaging the results.

We refer to our proposed elastography method as Mixed-PDE.

Finally, our proposed pipeline to measure relative-stiffness maps from images consists in the successive combination of our HTV OF method (to measure deformation from images) and our Mixed-PDE elastography method (to invert the stiffness from the deformation).

IV. Experiments With Simulated Data

In this section, we first describe the simulation framework, the experimental setups, and the performance metrics that we use for the evaluation of the algorithms. We then test the accuracy of our proposed methods in several different ways.

- First, we study how well our proposed OF recovers displacement and strain fields from images.
- Second, given the displacements, we compare our stiffness reconstruction algorithm to direct and indirect reconstruction methods.
- Third, we measure the accuracy of the entire pipeline and its effectiveness in recovering the heterogeneous stiffness of the cell nucleus from images.

Finally, we study the accuracy of the pipeline for large deformations, as well as the errors that it incurs when working with 2D slices of 3D volumes.

A. Description of the Simulations

Since there are no standardized benchmarks for our problems, we use simulations as ground truth. The simulation pipeline goes as follows.

i. We choose an experimental setup (see Section IV-B). We define the domain of the nucleus and generate a mesh thereon. We then choose some boundary conditions and a map of stiffness, and solve (1) for the displacement using the FEM. We use triangular elements with six nodes. Each (square) pixel of the image is made up of two such elements. The mixed-formulation in (1) is meant to avoid locking effects [72].

ii. We interpolate the displacement field resulting from (i) onto the image domain, and use it to warp (third-order splines) a first image into a second one. We then add white Gaussian noise to both. These two images are the input to the algorithm that we want to evaluate.

We use (i) to evaluate the elastography methods alone and (i)-(ii) to evaluate the OF methods and the full pipeline.

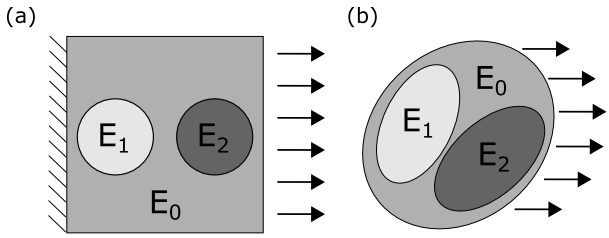

Fig. 2. Two examples of simulated experimental settings. The values E_0, E_1, E_2 denote the stiffness of the background and of the two inclusions (respectively), the arrows represent the applied traction on the boundary, and the lines represent the clamping. We use (a) in Figures 3-5 because it is more general to elastography (e.g., medical), and we use (b) in Figure 10 for an experiment that is closer to potential real conditions involving the nucleus.

B. Description of the Experimental Setups

We simulate three main experimental setups to test the accuracy of the reconstruction algorithms.

- *Inclusions.* In this setup, we consider an elastic material with a homogeneous stiffness (E_0) everywhere except at some inclusions. In Figure 2a, we show only two inclusions (of stiffness E_1, E_2), but we perform experiments with three inclusions as well. To deform the material, we apply a constant traction force from one side while the other side remains clamped.
- *Heterochromatin.* In this setup (Figure 2b), the heterochromatin gathers around a nucleolus, whereas the euchromatin stays loose in a highly transcriptive domain. To represent this, we model the nucleus as an ellipsoid of stiffness 1 with two elliptic inclusions of stiffness 0.2 and 5. We apply traction to this configuration from one side.
- *Lamina.* This setup represents heterochromatin that has gathered around the nuclear-pore complexes at the periphery. As a result, the boundary and its neighborhood is five times stiffer than the inside. The nucleus is taken to be circular, as is the case for white blood cells. We apply traction to this configuration from one side.

On one hand, we use the Inclusions experiment to assess the OF and elastography methods individually because they are classical tests in standard elastography and because the inclusions could be likened to organelles in a nuclear-stiffness problem. On the other hand, and for lack of precedent, we designed the Heterochromatin and Lamina setups to test the pipeline in a setting that is more similar to real experiments (cf. Section V).

Authorized licensed use limited to: EPFL LAUSANNE. Downloaded on March 24,2025 at 15:29:48 UTC from IEEE Xplore. Restrictions apply.

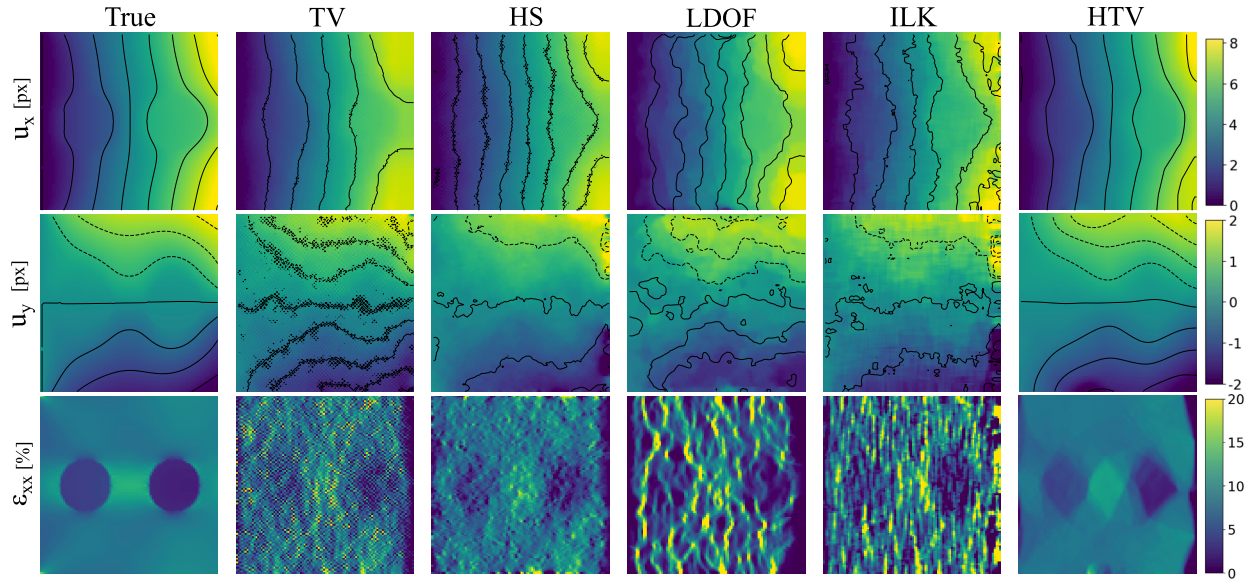

Fig. 3. Axial displacements, lateral displacements, and axial strain estimated from simulated images of the setup in Figure 2a using different optical-flow methods (ours is HTV). Level lines are plotted in black. The dimension of the images is (100 × 100). We added noise to them (PSNR 30 dB, or SNR 20 dB). We chose this PSNR to reflect that of a common confocal image. Here, the first inclusion has a relative stiffness value of 3, the second of 5, and the background of 1. Both inclusions have a radius of 15 pixels. Poisson's ratio is set to 0.3. There is another example in Figure S3.

TABLE II

RMSE AND CNR OF THE STRAIN FIELD FOR EXPERIMENTS WITH VARYING STRETCHING CONDITIONS (SEE SECTION IV-B). WE EVALUATED THE CNR OVER A (5 × 5) SQUARE WITHIN THE STIFFEST INCLUSION AND A SQUARE OF EQUAL SIZE CENTERED AROUND (75, 75). THE DIMENSION OF THE IMAGES IS (100 × 100). WE ADDED NOISE TO THEM (PSNR 30 dB)

	RMSE ε [%]				CNR ε [a.u.]			
OF	T	ν	E	Nb. inc.	T	ν	E	Nb. Inc.
HTV	$\mathbf{0.51 \pm 0.11}$	$\mathbf{0.53 \pm 0.09}$	$\mathbf{0.57 \pm 0.01}$	$\mathbf{0.58 \pm 0.08}$	$\mathbf{48.25 \pm 27.37}$	$\mathbf{122.07 \pm 95.02}$	$\mathbf{101.07 \pm 85.72}$	$\mathbf{124.32 \pm 115.33}$
TV	2.16 ± 0.06	2.19 ± 0.06	2.20 ± 0.06	2.21 ± 0.06	0.80 ± 0.54	1.07 ± 0.50	0.97 ± 0.53	1.01 ± 0.51
HS	0.95 ± 0.16	1.10 ± 0.20	1.14 ± 0.17	1.15 ± 0.16	5.88 ± 4.31	7.78 ± 4.20	8.97 ± 5.75	10.47 ± 6.32
LDOF	2.00 ± 0.46	2.29 ± 0.56	2.47 ± 0.49	2.61 ± 0.54	0.74 ± 0.38	0.70 ± 0.29	0.80 ± 0.53	1.28 ± 1.48
ILK	1.10 ± 0.35	1.24 ± 0.22	1.32 ± 0.25	1.36 ± 0.25	5.98 ± 3.33	6.02 ± 2.56	5.68 ± 2.92	6.52 ± 4.59

To test the accuracy of the methods in a wider range of conditions, we will take the average (and standard deviation) of the accuracy over many experiments. More specifically, for the Inclusions, we take them over the traction magnitudes $\mathbf{T} \in \{0.03, 0.05, 0.07, 0.09\}$, Poisson's ratios $\nu \in \{0.3, 0.33, \ldots, 0.45\}$ [73], [74]; stiffness of the inclusions $(E_1, E_2) \in \{(3, 3), (3, 4), \ldots, (3, 8)\}$, and number of inclusions $\{1, 2, 3\}$. For the latter, the stiffness ratios (background to inclusions) are 1 to $\{3\}$, 1 to $\{3, 5\}$, and 1 to $\{3, 5, 7\}$. For the Heterochromatin and Lamina configurations, we take the statistics over the same range of Poisson's ratios and over a range $\mathbf{T} \in \{0.03, 0.04, 0.05, 0.06\}$ of traction magnitudes. In addition, we consider a third variation that we call "BC". It consists on a variation of the extent of the zone of application (see Figure 2b) of the traction forces (from $\{30, 50, 70, 90\}$% of the perimeter).

We remark that all experiments are in 2D unless stated otherwise.

C. Description of the Performance Metrics

We test the accuracy of the methods according to three different metrics.

- The root-mean-square error (RMSE) of the displacements, the strain, or the stiffness.
- The contrast-to-noise ratio (CNR) between the stiffnes or strain of two regions. For example, if h stands for the heterochromatin region and e for the lamina one, then $\text{CNR} = \sqrt{(\overline{s^{\text{h}}} - \overline{s^{\text{e}}})^2/(\sigma_{\text{h}}^2 + \sigma_{\text{e}}^2)}$. Here, $\overline{s^{\bullet}}$ and $\sigma_{\bullet}$ stand for the mean and standard deviation of the stiffness or strain, respectively. Larger values are better.
- The mean value of the reconstructed stiffness over a region of interest. For example, m_{h} and m_{e}. The best m is the one that gets the closest to the mean of the ground truth.

D. Reconstruction of Deformations From Images

We compared our HTV displacement-estimation method to the following OF techniques: Horn and Schunck (HS) [40], TV-L_1 [75], large-displacement OF (LDOF) [64], and iterative Lukas-Kanade (ILK) [76]. LDOF combines descriptor matching with TV-L_1 OF. For all methods, we performed a grid search to find the best hyperparameters.

We tested the accuracy of the OF methods on the Inclusions setup (Figure 2a). In Figure 3, we show the lateral displace-

Authorized licensed use limited to: EPFL LAUSANNE. Downloaded on March 24,2025 at 15:29:48 UTC from IEEE Xplore. Restrictions apply.

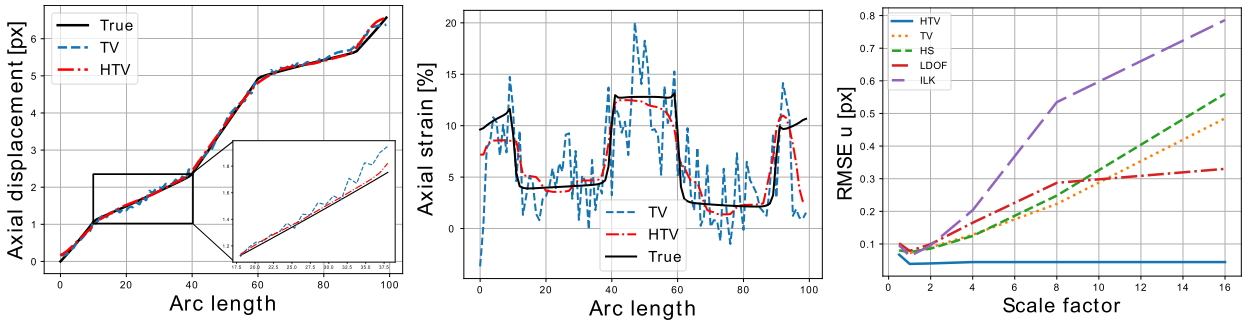

Fig. 4. Left and middle: cross-section along the x axis at $Y = 50$ of the axial displacement (which is piecewise-linear as per the linear-elasticity equations) and the corresponding axial strain in Figure 3. The cross-section is taken along the same direction in which the traction is applied to the setup. Our HTV regularization of OF is compared to the widespread TV regularization, which suffers from staircasing. We applied large tractions to test the method thoroughly. There is another example in Figure S3. Rightmost: RMSE of the displacement as function of the regularization parameter. The dimension of the images is (100 × 100). We added noise to them (PSNR 30 dB).

TABLE III

RMSE OF THE RECONSTRUCTIONS OF THE RELATIVE STIFFNESS MAP FOR DIFFERENT STRETCHING CONDITIONS (SEE SECTION IV-B). ALL ELASTOGRAPHY METHODS WERE INPUTTED THE TRUE DISPLACEMENT FIELD WITH ADDITIONAL NOISE (PSNR 30 dB)

Method	RMSE relative stiffness (10^{-2}) [a.u.]			
	T	ν	E	Nb. inc.
Dir.	85.02 ± 0.00	85.46 ± 1.43	65.45 ± 12.20	59.39 ± 19.30
Dir. rel.	82.25 ± 0.00	78.42 ± 2.77	60.43 ± 13.66	49.98 ± 20.73
Indirect	78.29 ± 3.46	81.62 ± 5.66	60.69 ± 14.03	55.20 ± 26.62
Ind. rel.	79.21 ± 0.77	$\mathbf{71.47 \pm 5.00}$	69.96 ± 5.54	73.59 ± 13.46
Mixed PDE	$\mathbf{74.06 \pm 1.89}$	77.57 ± 2.77	$\mathbf{54.58 \pm 12.11}$	$\mathbf{41.41 \pm 18.42}$

ments, the axial displacements, and the axial strain recovered by the different OF methods. Our HTV method captured the displacements well, eliminating the staircasing seen in TV-based methods. As a result, the strain computed therefrom was much less noisy, which could potentially improve the determination of the stiffness. These observations were even more clear in the 1D profiles (Figure 4) that cut across the two inclusions. There, we could see that our method recovers the continuous and piecewise linear behavior of the axial displacements, with the slopes being inversely proportional to the value of the stiffness.

To make the evaluation more quantitative, we then computed the RMSE of the displacements and the strain (CNR too) under different boundary conditions, Poisson's ratios, as well as stiffness and number of inclusions. The results in Tables I and II confirmed our visual inspection of Figures 3-4: our proposed OF outperformed the other methods in the recovery of deformations that derive from elasticity problems.

Next, we assessed the sensitivity to noise of the OF methods. To this end, we added increasing levels of Gaussian noise to the two images used for the reconstruction (Figure 5). HTV outperformed the other OF methods throughout the range of noise tested. The noise sensitivity of the strain recovered by HTV was particularly low compared to the alternatives.

An additional illustration of our HTV reconstruction with different boundary conditions can be found in the Supplementary (Figure S3).

Lastly, we studied the effect of the regularization parameter on the reconstructions. The rightmost panel in Figure 4 shows that our method was quite robust to the choice of parameter,

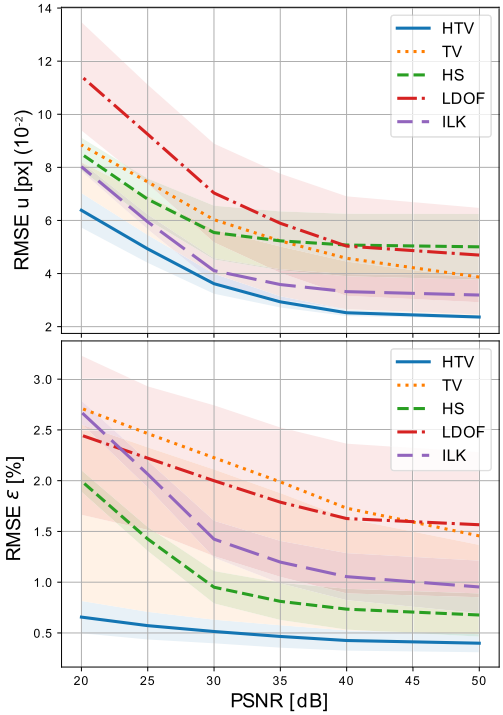

Fig. 5. Top: evolution of the RMSE of the displacement field of several OF methods as a function of noise (PSNR of the image). The shading reflects the standard deviation resulting from different experiments with varying traction forces. The SNRs of these images were rather consistently around 5 dB below their PSNR. Bottom: same as on top but with the strain field.

in part due to sparsity. This also means that the grid search was more beneficial for the competing methods than for our HTV.

E. Reconstruction of Stiffness From Deformations

We compared our Mixed-PDE stiffness-reconstruction framework to direct [17] and indirect [18] elastography methods. We considered two versions for each method: one for which the tractions are known, and one for which they are not. We refer to the latter version as "relative". In the "relative" case, the traction forces are derived from the displacement at

Authorized licensed use limited to: EPFL LAUSANNE. Downloaded on March 24,2025 at 15:29:48 UTC from IEEE Xplore. Restrictions apply.

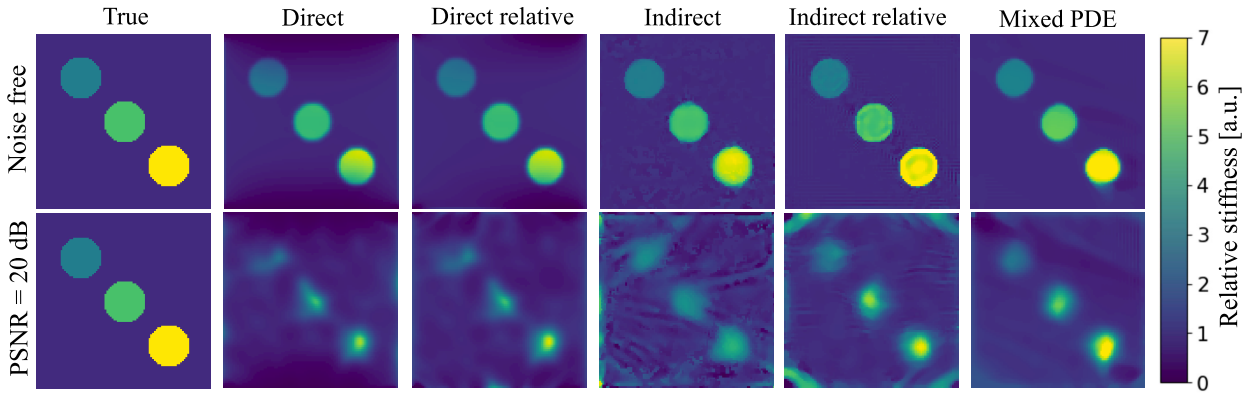

Fig. 6. Comparison of all elastography methods in the reconstruction of the relative stiffness of three stiff inclusions given the same displacements, without (first line) or with (second line) additional noise. We added noise to reach a PSNR of 20 dB. This PSNR was chosen lower to reflect the process of having already estimated the displacements. Images are of dimension (100×100). Each inclusion has a radius of 12 pixels. The relative stiffness of the background to the inclusions is 1 to 3, 5, 7. Traction is applied on both the left and right borders of the image (see Figure S2). The point-wise maximum of the inputted displacement is 3 pixels. Poisson's ratio is set to 0.3.

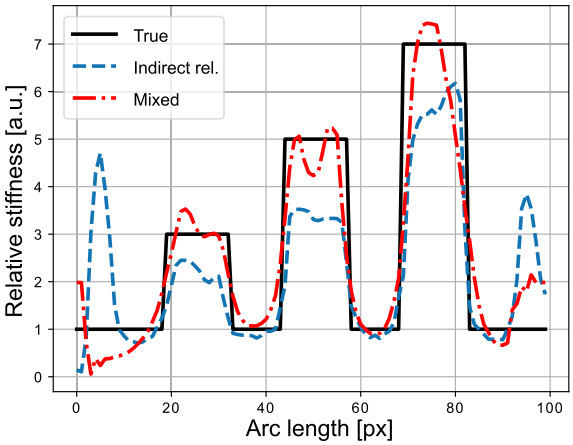

Fig. 7. Cross-sections along the diagonal of the stiffness map in Figure 6 for the two most accurate elastography methods.

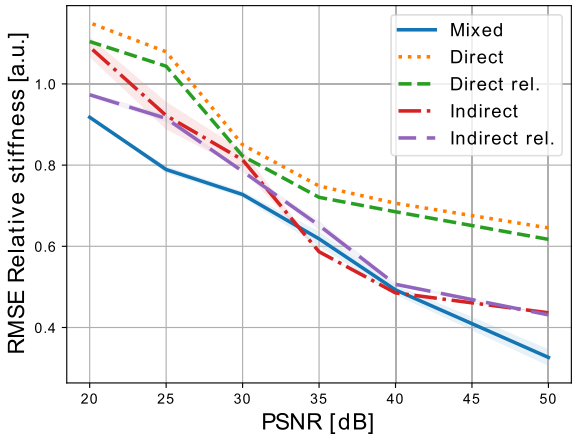

Fig. 8. RMSE of the elastography methods as a function of noise (PSNR of the displacement field). The shading reflects the standard deviation resulting from experiments with varying traction forces. The SNRs of these displacement fields were rather consistently around 3 dB below their PSNR.

the boundary. In principle, this is the only possibility for freely deforming cells.

We tested the accuracy of the elastography methods on the Inclusions setup. In Figure 6, we show the reconstruction of the stiffness for an experiment with three inclusions. All methods were able to recover the position and shape of the inclusions. However, the relative stiffness was underestimated for the direct and indirect "relative" methods. This was slighlty improved when the boundary forces are known (lack of "relative"). Our Mixed PDE was more accurate than the competing methods without requiring knowledge of the boundary traction. This was all clearer in the one-dimensional profiles (Figure 7). Note, however, that this was likely due to the fact that we assume that the stiffness of the boundary is homogeneous.

To make the evaluation more quantitative, we computed the RMSE of the stiffness for the different conditions of the experimental setup. The results (Table III) showed that the Mixed-PDE method outperformed the indirect relative method in many cases while being significantly faster (Table IV).

TABLE IV
RUNTIME OF OUR MIXED-PDE METHOD COMPARED TO AN INDIRECT RECONSTRUCTION. A SINGLE CPU WAS USED FOR EACH EXPERIMENT. THE EXPERIMENTS WERE PERFORMED FOR THE SETUP WITH THREE INCLUSIONS IN FIGURE 6

Number of Nodes	Indirect	Mixed PDE
(100×100)	9min 14s	2.7s
(500×500)	7h 19 min 59s	26s
(1000×1000)	1d 3h 58 min 42s	2min 37s

Indeed, indirect methods seemed to become intractable very soon.

Our noise-sensitivity analysis (addition of noise to the input displacements) showed that all methods are sensitive to a similar extent (Figure 8).

F. Reconstruction of Stiffness From Images (Pipeline)

We then tested the full reconstruction pipeline: an OF method to reconstruct the displacements from a pair of images followed by a method to recover the stiffness therefrom.

Authorized licensed use limited to: EPFL LAUSANNE. Downloaded on March 24,2025 at 15:29:48 UTC from IEEE Xplore. Restrictions apply.

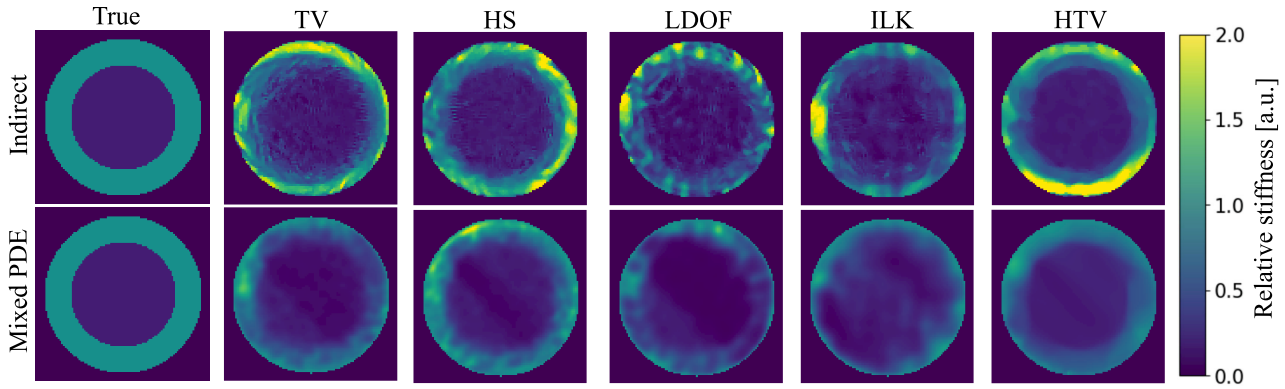

Fig. 9. Combination of OF methods (columns) with elastography methods (rows) for the reconstruction of stiffness maps from images. The simulated experiment corresponds to the Lamina configuration. Our proposed combination is at the bottom right corner (HTV + Mixed-PDE). The dimension of the images is (100 × 100). We added noise to them (PSNR 30 dB). Traction was applied to 90% of the boundary. The point-wise maximal displacement field is 5 pixels. The Poisson's ratio is set to 0.3.

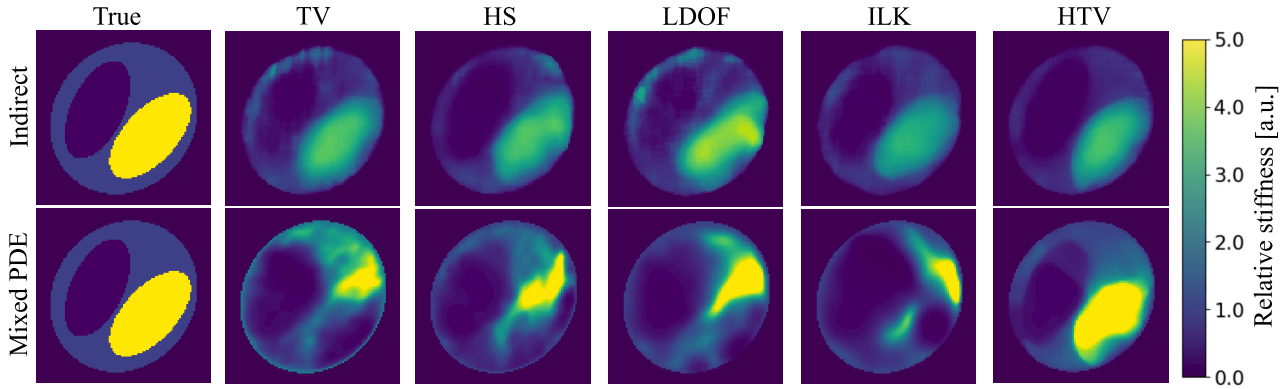

Fig. 10. Combination of OF methods (columns) with elastography methods (rows) for the reconstruction of stiffness maps from image pairs. The simulated experiment corresponds to the Heterochromatin configuration. Our proposed combination is at the bottom right corner (HTV + Mixed-PDE). The dimension of the images is (100 × 100). We added noise to them (PSNR 30 dB). Traction was applied to 90% of the boundary. The point-wise maximal displacement field is 5 pixels. The Poisson's ratio is set to 0.3.

We tested the accuracy of the OF methods on both the Lamina (Figure 9) and Heterochromatin (Figure 10) setups. We tested multiple combinations of OF and relative-elastography methods by applying (unknown) traction forces to either configuration. For all methods, we performed a grid search to find the best hyperparameters, which helped the competing OF methods more than it helped ours.

The combination of our proposed HTV-based OF with our Mixed-PDE method was the most accurate overall, even if HTV+Indirect was occasionally better, especially in the Heterochromatin configuration (Figures 9, 10). The two combinations could differentiate the stiffness of the different structures within the nucleus and their approximate location, albeit with some smoothing at the boundaries of the inclusions. However, the mixed-PDE was generally better at recovering the actual (relative) stiffness values, possibly due to the assumption of homogeneity over the boundary. We remark that the estimation of stiffness from images is a difficult problem in general. Even in ideal conditions where the traction is known and the image coincides with the elastic domain, the stiffness is often underestimated [19].

In almost all cases, the two elastography methods did better when using the displacements that result from our HTV-based method. To make the evaluation more quantitative, we computed the RMSE, CNR, and mean values under different conditions. Note that the last two metrics are a measure of how distinguishable the different domains inside the nucleus are, which, in turn, reflects diagnostic value. The results of this analysis can be found in Tables V, VI. They are in agreement with our visual analysis.

Lastly, we assessed the sensitivity of the pipelines to image noise. We used the Lamina setup for this purpose because we deemed it a more likely configuration in real experiments. The combination of Mixed-PDE and HTV was more accurate over the noise range that we tested, as well as over all the parameter variations of the setup (Figure 11).

G. Accuracy for Large Deformations

Linear elasticity is only a good approximation when the strain is small. To study the effect of large deformations on our inverse problem, we used a hyper-elastic model (see Appendix D) for comparison.

Authorized licensed use limited to: EPFL LAUSANNE. Downloaded on March 24,2025 at 15:29:48 UTC from IEEE Xplore. Restrictions apply.

TABLE V

WHOLE PIPELINE FOR THE LAMINA CONFIGURATION. RMSE, m_{I} (TARGET VALUE AT THE INTERIOR OF THE NUCLEUS), m_{B} (TARGET VALUE AT THE BOUNDARY OF THE NUCLEUS) AND CNR OF THE RECONSTRUCTED STIFFNESS FOR THE COMBINATION OF ALL OF METHODS (OURS IS HTV) WITH THE TWO MOST ACCURATE ELASTOGRAPHY METHODS: RELATIVE INDIRECT, AND OUR MIXED PDE. THE STATISTICS ARE TAKEN OVER SEVERAL VARIATIONS OF THE SETUP (SEE SECTION IV-B). THE DIMENSION OF THE IMAGES IS (100 × 100). WE ADDED NOISE TO THEM (PSNR 30 dB)

Experiments		Indirect					Mixed PDE				
		HTV	TV-L1	HS	LDOF	ILK	HTV	TV-L1	HS	LDOF	ILK
T	RMSE	0.22 ± 0.01	0.26 ± 0.01	0.28 ± 0.01	0.27 ± 0.00	0.28 ± 0.02	**0.16 ± 0.01**	0.26 ± 0.01	0.22 ± 0.01	0.21 ± 0.01	0.23 ± 0.02
	m_{I} (0.2)	**0.20 ± 0.01**	0.21 ± 0.01	0.14 ± 0.02	0.18 ± 0.01	0.23 ± 0.01	0.24 ± 0.01	0.12 ± 0.03	0.19 ± 0.01	0.24 ± 0.02	0.23 ± 0.03
	m_{B} (1.0)	0.75 ± 0.01	0.77 ± 0.03	0.62 ± 0.03	0.65 ± 0.01	0.68 ± 0.01	**0.78 ± 0.01**	0.52 ± 0.01	0.62 ± 0.02	0.64 ± 0.02	0.59 ± 0.03
	CNR	4.08 ± 0.6	2.58 ± 0.29	2.67 ± 0.33	2.26 ± 0.06	1.80 ± 0.04	**8.93 ± 0.73**	5.67 ± 0.17	6.67 ± 0.29	6.85 ± 0.30	5.15 ± 0.58
ν	RMSE	0.21 ± 0.01	0.24 ± 0.01	0.27 ± 0.01	0.26 ± 0.01	0.25 ± 0.02	**0.17 ± 0.00**	0.33 ± 0.06	0.28 ± 0.06	0.25 ± 0.03	0.26 ± 0.03
	m_{I} (0.2)	0.19 ± 0.01	0.21 ± 0.01	0.14 ± 0.01	**0.20 ± 0.01**	0.26 ± 0.03	0.22 ± 0.01	0.07 ± 0.04	0.12 ± 0.06	0.18 ± 0.03	**0.20 ± 0.01**
	m_{B} (1.0)	0.76 ± 0.02	0.79 ± 0.03	0.63 ± 0.04	0.68 ± 0.02	0.76 ± 0.06	**0.82 ± 0.06**	0.37 ± 0.13	0.48 ± 0.13	0.54 ± 0.06	0.54 ± 0.04
	CNR	4.08 ± 0.59	2.58 ± 0.29	2.67 ± 0.33	2.26 ± 0.05	1.80 ± 0.04	**8.73 ± 1.52**	3.54 ± 1.80	4.60 ± 1.79	4.47 ± 1.72	3.53 ± 1.38
BC	RMSE	0.24 ± 0.02	0.28 ± 0.02	0.28 ± 0.01	0.29 ± 0.02	0.29 ± 0.01	**0.17 ± 0.02**	0.26 ± 0.01	0.20 ± 0.01	0.25 ± 0.03	0.26 ± 0.02
	m_{I} (0.2)	**0.20 ± 0.01**	0.19 ± 0.01	0.15 ± 0.02	0.17 ± 0.01	0.19 ± 0.01	0.22 ± 0.02	0.15 ± 0.02	0.26 ± 0.07	0.16 ± 0.06	0.19 ± 0.04
	m_{B} (0.2)	0.75 ± 0.04	0.72 ± 0.02	0.64 ± 0.05	0.70 ± 0.07	0.68 ± 0.02	**0.80 ± 0.04**	0.52 ± 0.02	0.67 ± 0.04	0.54 ± 0.06	0.52 ± 0.04
	CNR	3.16 ± 0.93	2/04 ± 0.43	2.42 ± 0.07	2.24 ± 0.37	1.91 ± 0.29	**9.65 ± 1.02**	5.43 ± 0.29	6.20 ± 0.22	5.22 ± 0.81	3.65 ± 0.98

TABLE VI

WHOLE PIPELINE FOR THE HETEROCHROMATIN CONFIGURATION. RMSE, m_{e} (TARGET VALUE OF THE EUCHROMATIN REGION), m_{h} (TARGET VALUE AT THE HETEROCHROMATIN REGION) AND CNR OF THE RECONSTRUCTED STIFFNESS FOR THE COMBINATION OF ALL OF METHODS (OURS IS HTV) WITH THE TWO MOST ACCURATE ELASTOGRAPHY METHODS: RELATIVE INDIRECT, AND OUR MIXED PDE. THE STATISTICS ARE TAKEN OVER SEVERAL VARIAITONS OF THE SETUP (SEE SECTION IV-B). THE DIMENSION OF THE IMAGES IS (100 × 100). WE ADDED NOISE TO THEM (PSNR 30 dB)

Experiments		Indirect					Mixed PDE				
		HTV	TV-L1	HS	LDOF	ILK	HTV	TV-L1	HS	LDOF	ILK
T	RMSE	0.71 ± 0.07	1.05 ± 0.04	1.06 ± 0.05	1.17 ± 0.04	1.23 ± 0.00	**0.61 ± 0.02**	1.43 ± 0.01	1.26 ± 0.01	1.28 ± 0.01	1.45 ± 0.05
	m_{e} (0.2)	0.27 ± 0.02	0.43 ± 0.06	0.20 ± 0.01	0.88 ± 0.07	0.50 ± 0.05	0.30 ± 0.02	0.12 ± 0.01	**0.26 ± 0.02**	0.27 ± 0.04	0.13 ± 0.06
	m_{h} (5.0)	3.16 ± 0.29	2.00 ± 0.20	1.82 ± 0.20	1.71 ± 0.13	1.29 ± 0.03	**4.11 ± 0.08**	0.41 ± 0.02	0.93 ± 0.02	0.89 ± 0.05	0.34 ± 0.16
	CNR	**15.39 ± 1.89**	6.92 ± 2.19	10.75 ± 1.49	0.99 ± 0.46	1.79 ± 0.37	10.51 ± 0.76	4.63 ± 0.67	4.73 ± 2.93	5.73 ± 2.08	5.13 ± 4.16
ν	RMSE	0.68 ± 0.07	1.06 ± 0.04	1.04 ± 0.03	1.21 ± 0.11	1.17 ± 0.05	**0.63 ± 0.01**	1.51 ± 0.06	1.38 ± 0.12	1.27 ± 0.03	1.53 ± 0.03
	m_{e} (0.2)	**0.28 ± 0.02**	0.43 ± 0.06	0.29 ± 0.10	0.84 ± 0.02	0.61 ± 0.13	0.29 ± 0.01	0.06 ± 0.04	0.15 ± 0.08	0.43 ± 0.37	0.08 ± 0.01
	m_{h} (5.0)	3.32 ± 0.20	1.90 ± 0.21	1.89 ± 0.09	1.53 ± 0.41	1.50 ± 0.15	**4.04 ± 0.02**	0.20 ± 0.16	0.59 ± 0.35	0.94 ± 0.11	0.11 ± 0.09
	CNR	**15.38 ± 1.88**	6.92 ± 2.19	10.75 ± 1.49	0.99 ± 0.46	1.79 ± 0.04	9.76 ± 0.35	4.63 ± 0.67	25.73 ± 5.94	5.73 ± 2.08	5.13 ± 4.16
BC	RMSE	0.77 ± 0.09	1.03 ± 0.02	1.03 ± 0.05	1.19 ± 0.05	1.22 ± 0.02	**0.74 ± 0.19**	1.43 ± 0.02	1.26 ± 0.02	1.30 ± 0.04	1.46 ± 0.04
	m_{e} (0.2)	0.32 ± 0.03	0.28 ± 0.14	**0.18 ± 0.02**	0.64 ± 0.28	0.34 ± 0.11	0.31 ± 0.02	0.17 ± 0.05	0.31 ± 0.07	0.40 ± 0.34	0.12 ± 0.04
	m_{h} (5.0)	2.92 ± 0.46	1.92 ± 0.10	1.94 ± 0.19	1.38 ± 0.34	1.28 ± 0.07	**4.03 ± 0.37**	0.42 ± 0.04	0.94 ± 0.07	0.82 ± 0.14	0.31 ± 0.17
	CNR	**13.47 ± 2.45**	10.96 ± 3.74	9.92 ± 1.08	2.59 ± 2.06	2.98 ± 1.05	9.11 ± 3.41	4.34 ± 1.24	8.21 ± 3.50	7.50 ± 5.78	4.16 ± 2.44

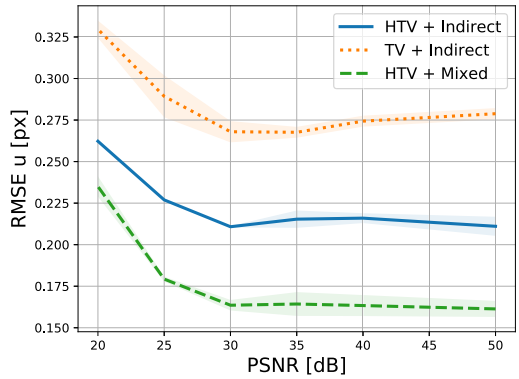

Fig. 11. RMSE of the combination of two OF techniques (TV or our HTV) with our Mixed PDE or with indirect elastography against increasingly noisy images. This was evaluated over experiments with varying traction forces.

We first studied the behavior of the Mixed-PDE method alone. We performed two alternative simulations of the setting in Figure 9, either with the linear elastic model (1) or with the hyper-elastic model (13). We then inputted the resulting "true" displacements to the Mixed-PDE method, which uses a linearly elastic model, to invert for the stiffness.

The accuracy of the reconstruction when the underlying truth is hyper-elastic worsened as the strain increased, whereas it remained stable when the truth was linear because the models matched (Figure 13). However, the difference in accuracy was modest over the range of strains that we tested.

Next, we tested our HTV + mixed-PDE pipeline. In this case, instead of inverting the true displacements resulting from the two alternative simulations, we used the displacements to warp an image as described in Section IV-A. We then used our HTV method to estimate the displacements from the images and subsequently inverted them for the stiffness using the Mixed-PDE method.

For the full pipeline, the accuracy of the reconstruction worsened as the strain increased for both the linear and hyper-elastic models, and the difference between them was reduced (Figure 13).

We remark that one can design experiments where deformations are small. For freely moving cells, one could simply wait for the deformations to be small; whereas, for cells that are being actively manipulated, one can adjust the magnitude of the probing.

H. Accuracy for 2D Slices of 3D Bodies

We focused on 2D in the development of our method because cells are often imaged in 2D. (Anyway, 3D acquisi-

Authorized licensed use limited to: EPFL LAUSANNE. Downloaded on March 24,2025 at 15:29:48 UTC from IEEE Xplore. Restrictions apply.

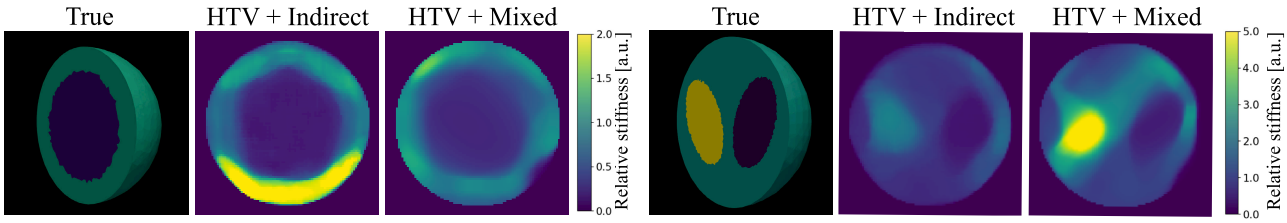

Fig. 12. 2D reconstructions of a 3D simulation (True, ($100 \times 100 \times 100$)) given a 2D image slice (100×100) of the simulated 3D volume. We added noise to them (PSNR 30 dB). A 10% of the boundary is clamped, the rest has a normal traction applied to it. The point-wise maximal displacement field is 3 pixels for the configuration on the left, and 5 for the configuration on the right. The Poisson's ratio is set to 0.3.

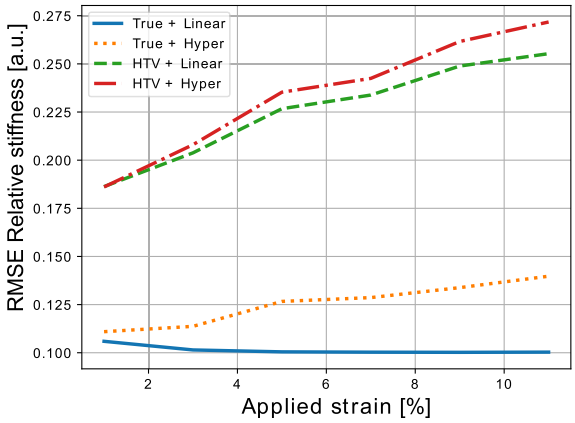

Fig. 13. RMSE of the relative stiffness reconstructed as a function of the strain applied in simulations of a linearly elastic model (Linear) or a hyper-elastic (Hyper) model. For the "True" label, the Mixed-PDE method is applied to the true displacements. For the "HTV" label, the Mixed-PDE method is applied to the displacements resulting from our HTV method. This is for the Lamina configuration.

tions might be too slow to accurately capture the deformations of the cell.) However, cells are truly 3D bodies.

Therefore, we tested whether the stiffness maps recovered by our method from 2D images are representative of the 3D stiffness of the cell. To this end, we performed the same simulations described in Section IV-A, but in 3D by means of the 3D FEM followed by 3D warping. We then took a 2D slice from the 3D volume both before and after the deformation and applied our HTV+Mixed-PDE pipeline thereto, thus reconstructing a 2D stiffness slice.

For the spherical versions of the stiff-lamina and of the stiff-chromatin configurations, the 2D stiffness maps estimated from the sliced images reflected well the main features of the true 3D stiffness (Figure 12).

Unfortunately, this might not apply to slices that are offset from the center, or when the stiffness is much more heterogeneous. To deal with these special cases when imaging in 3D is feasible, and also for completeness, we provide a proof of concept for the extension of our method to 3D in Appendix E.

V. Experiments With Real Data

We applied our proposed method (HTV + Mixed-PDE) to real data of deforming nuclei. To this end, we first applied our HTV OF on the images. In this way, the image derivatives necessary for the data term were able to consider information (also) from around the regions of interest (the nuclei). Next, we readily segmented the fluorescent nuclei using an active-contours algorithm. We then constrained the displacements and the reconstruction domain of our Mixed-PDE algorithm to the segmented nuclei where the elastic model holds. Thus, the stiffnesses that we reconstructed were constrained to the nuclei.

We first considered the nucleus of an SKOV3 cell under an AFM probe. (The data were from [73].) The nucleus is labelled with a fluorescence marker and imaged with a modified light-sheet microscope. The normal procedure here would be to measure the length of the deformation and derive a single value of stiffness. Instead, we applied our method to the images (Figure 14, top row). The reconstructed stiffness was higher around the boundary, which likely outlines the lamina. We found the stiffness ratio between the lamina and the innermost part to be 1.33. In comparison, the authors of [73] found stiffness values that led to a ratio of 1.36. They did so by simulating the compression using a shell model of the lamina while matching the change in perimeter and volume to that of the real data. Since the deformation of the SKOV3 cell is fairly large, one should consider these results in light of Section IV-G.

This experiment [73] is a great platform to test the combination of our microscopy-based technique with a probing technique. Since the force applied by the cantilever is known (~ 5 nN), we can try to make our relative-stiffness maps specific (i.e., provide units). As a proof of concept, we compared this force to the approximation $c|\Omega|^{-1}a\int_\Omega E(\mathbf{r})\varepsilon_{22}(\mathbf{r})\mathrm{d}\mathbf{r}$, where a is the cross-sectional area and we considered the strain in the direction of the applied force. This yields a scaling of $c = 0.64$ kPa for the top row of Figure 14.

We also studied freely deforming cardiomyocytes because they compress naturally (Figure 14, bottom row). The data were from the authors of [20], [77], and [78]. In this case, we found two main regions of stiffness with a ratio of 9.41. In [20], they used segmentation to divide the image approximately into heterochromatin and euchromatin, each with a constant stiffness. In agreement with our estimates, the authors found 10 to be the ratio that best explains the deformation given the two segmented regions.

VI. Discussion

The performance of our HTV OF method highlights how important it is to adapt the regularization to the context at hand. We achieved this by incorporating a regularization

Authorized licensed use limited to: EPFL LAUSANNE. Downloaded on March 24,2025 at 15:29:48 UTC from IEEE Xplore. Restrictions apply.

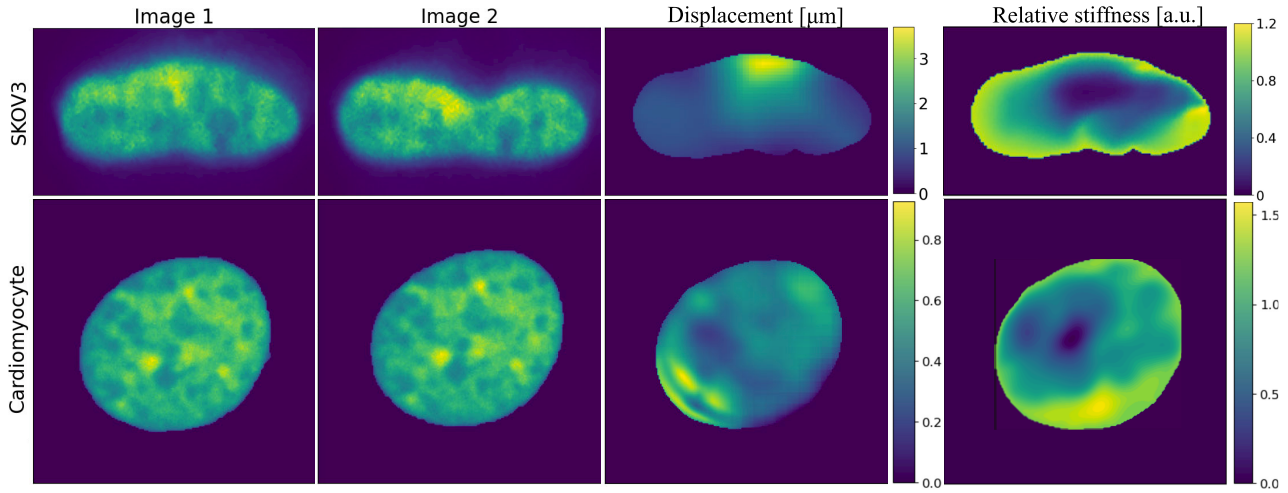

Fig. 14. Reconstruction of the stiffness of the nucleus of SKOV3 cells and of cardiomyocytes from images using our pipeline (HTV+Mixed-PDE). The displacements are constrained to the segmentations of the nuclei used by the Mixed-PDE algorithm for the reconstructions of the stiffnesses. SKOV3 data are taken directly from [73], and cardiomyocyte data from [20], [77], and [78]. The SKOV3 data were acquired at 0.14 μm/px using a light-sheet microscope with a UplanSAPO 60x/1.2 NA W objective from Olympus [79]. The width of the images is 25 μm and their dimension is (106×181). The force applied by the AFM was roughly 5 nN in the vertical direction. The cardiomyocyte data were acquired at 0.15 μm/px using an inverted epifluorescence microscope with a Plan Fluor 100x/1.30 NA Oil objective from Nikon. The width of the images is 30 μm and their dimension is 201×201.

that promotes continuous piecewise-linear displacements. As a result, the displacements are closer to those expected from the elasticity equations and are more amenable to differentiation into strain fields. In turn, this translates into a better accuracy of the elastography inversion and into a greater tolerance to noise, making the faster Mixed-PDE method more widely applicable.

The speed of the Mixed-PDE method is crucial to the application of elastography methods to the large datasets that are common in biology; for example, when experiments (such as those in Section V) are repeated over large populations or over different conditions, or when data are acquired in 3D. One disadvantage of the Mixed-PDE method, however, is that it assumes that the Young's modulus is homogeneous at the border. While this assumption is convincing for the nucleus because it is surrounded all over by the same material, it might not extend well to other situations or disciplines. When homogeneity cannot be assumed, one might want to revert to indirect methods. In this direction, one possibility would be to optimize the OF and elastography functionals jointly. While this kind of combinations has been investigated for other linear PDEs [80], the non-linearity that is required to assure that the Young's modulus remains positive would likely make them even slower.

A limiting factor of our elastography method is its reliance on a linear approximation, which is only good when the deformations are small. In many cases, fortunately, one can control the magnitude of the deformations, either by waiting in the case of freely moving cells, or by exerting a gentler traction in probing experiments. Therefore, future work will focus on the development of inversion techniques with more accurate models. Since elastography problems can be very ill-posed and OF appears to be less informed as the dimension grows, another perspective is to study the 3D inversion more thoroughly. This would be especially useful in cases where 2D slices are neither representative of the deformation nor of the stiffness of the whole volume of the cell (or of its nucleus).

Our HTV+Mixed-PDE pipeline can work on freely moving cells using fluorescence images alone. Since the forces that cause the deformations are unknown, the stiffness maps can only be recovered up to a constant. To make the maps quantitative one possibility is to combine the fluorescence imaging with other techniques. In this paper, we used the probing experiments in [73] as a proof of concept. However, another promising avenue might be to leverage the microenvironments of the cells. In particular, matrices with a calibrated behavior (e.g., collagen [81]) could serve as indirect probes while offering a more physiological environment for cells to move through. In this case, one could combine a model for the intracellular and the extracellular using constitutive equations and deformation-estimation methods in the same spirit as this paper.

VII. Conclusion

We presented a fast and robust method to measure intracellular stiffness with applications to the nucleus. The method is based on the combination of novel formulations of optical flow and of the inversion of the elasticity equations. It can be applied to freely deforming cells. And it does not require additional information such as the measurement of traction forces. We validated the method with simulations and confirmed its practical use with real data. In particular, we were able to distinguish different regions inside the nuclei of cardiomyocytes and ovarian cancer cells.

Appendix

A. Piecewise Linearity in the Linear Elasticity Equations

Consider $d = 1$ and recall that the divergence of the stress should be zero because there is no external force,

Authorized licensed use limited to: EPFL LAUSANNE. Downloaded on March 24,2025 at 15:29:48 UTC from IEEE Xplore. Restrictions apply.

$\nabla \cdot \varsigma = 0$. This means $\partial_x \left(p + 2\mu\varepsilon_{1,1}\right) = 0$, and thus $\varepsilon_{1,1}\partial_x E = -E\partial_x \varepsilon_{1,1}$ because $p = \mu\varepsilon_{1,1}$. If E is piecewise constant, then we can consider its derivative a Dirac comb with Diracs at the places where the stiffness changes. This means that a piecewise constant strain $\varepsilon_{1,1}(\mathbf{u})$ works as a solution. Therefore, a piecewise linear $\mathbf{u}$ is a solution of $\nabla \cdot \varsigma = 0$ as we wanted to show. This is a conceptual example to justify the framework, but axial displacements in the stiffness inclusions also appear to be piecewise linear in 2D.

This can be interpreted alternatively by thinking about a series of springs. Consider N springs with constant stiffness $(E_i)_{i\in\{1,\dots,N\}}$, strung in series at positions $(x_i)_{i\in\{1,\dots,N\}}$. The first end is fixed, and the last one is tethered to a constant traction force T. A simple integration of (1) yields a continuous piecewise-linear solution $u(x) = \sum_{i=1}^{N}\left[\frac{T}{E_i K}x + \sum_{k=1}^{i-1}\left(\frac{T}{E_k K} - \frac{T}{E_{k+1}K}\right)x_{k+1}\right]\chi_{[x_i,x_{i+1}]}(x)$, where $K = \frac{1-\nu}{(1+\nu)(1-2\nu)}$ is constant, and $\chi_{[x_i,x_{i+1}]}$ are indicator functions. The slope of the displacement field is inversely proportional to the stiffness of the material.

B. Lipschitz Constant of the Gradient of the Optical Flow Term

Consider $p = 2$ in (7) and denote D the ensuing differentiable image-data term. Let $\mathbf{u}, \mathbf{v}$ be two displacement fields, $\mathbf{J}_1 = \left(\partial_x I \partial_x I, \partial_x I \partial_y I\right)^T$, $\mathbf{J}_2 = \left(\partial_x I \partial_y I, \partial_y I \partial_y I\right)^T$, and let $||\cdot||$ stand for $||\cdot||_{\Omega_I,2}$. Then, we use

$$\|\nabla D(\mathbf{u}) - \nabla D(\mathbf{v})\| \leq 2\sqrt{\|\mathbf{J}_1\|^2 + \|\mathbf{J}_2\|^2}\,\|\mathbf{u} - \mathbf{v}\| \tag{12}$$

as a bound that is useful yet relatively fast to compute. We note that tighter bounds may be derived from the singular values of the Hessian of the image-data term.

C. Regularization Hyperparameter

Throughout the paper, we chose $\alpha_1 = \alpha_2$ as our go-to for the HTV hyperparameter. This was to mimic a situation where no information about the traction is known.

On the contrary, if there were an axial direction of traction (as is the case in Figure 3) and if it were known, then one could adopt $(\alpha_1, \alpha_2) = \lambda(1+\cos\theta, 1+\sin\theta)$ with $\lambda \in \mathbb{R}_{\geq 0}$ and with the angle $\theta \in [0, \pi/2]$ aligned with the traction. In principle, this would promote piecewise linearity more strongly along the axial direction (as one expects from the elasticity equations). Meanwhile, in typical elastography problems, the deformations that are perpendicular to the traction are smaller and more difficult to capture. Therefore, one might think of regularizing this perpendicular direction more to alleviate the ill-posedness. As a result of these two competing effects, the optimal regularization direction is not obvious and might be situational. In our experiments, we observed that the variations in RMSE across the directions were small. We surmise that this is due to of the robustness of the HTV hyperparameter (Figure 4-right).

While it is comparatively less important than for other OF methods because of this robustness (Figure 4-right), a complementary method to choose the regularization parameter could be Morozov's criterium, which requires an estimate of the noise in the image. Moreover, instead of simply scaling the hyperparameter at each of the scales of the OF multiresolution scheme, one could augment the regularization further by using adaptive multiscale regularization strategies [82].

D. Hyper-Elastic Model

Our hyper-elastic simulations follow a neo-Hookean model defined by the energy-minimization problem

$$\min_{\mathbf{u}}\left(\int_\Omega \psi(\mathbf{u})\mathrm{d}x - \int_{\Gamma_\mathbf{T}} \mathbf{T}\cdot\mathbf{u}\;\mathrm{d}s\right), \tag{13}$$

where $\psi(\mathbf{u})$ is the stored elastic energy defined by

$$\psi(\mathbf{u}) = \frac{\mu}{2}(I_c - 3) - \mu\ln(J) + \frac{\lambda}{2}\ln(J)^2, \tag{14}$$

with μ and λ the Lamé parameters, $\mathbf{F} = \nabla\mathbf{u} + \mathbb{1}$, $J = \det(\mathbf{F})$, $\mathbf{C} = \mathbf{F}^T\mathbf{F}$, and $I_c = \mathrm{tr}(\mathbf{C})$.

E. Extension of the Full Pipeline to 3D

1) Theory: The extension of problem (7) to 3D reads

$$\underset{\mathbf{u}\in \mathrm{BV}^{(2)}(\Omega_I,\mathbb{R}^d)}{\operatorname{argmin}}\left(\left|\left|\frac{\partial I}{\partial t} + \mathbf{u}\cdot\nabla I\right|\right|^p_{\Omega_I,p} + \sum_{k=1}^{d}\boldsymbol{\alpha}_k||\mathscr{H}\{\mathbf{u}_k\}||_{*,\mathscr{M}}\right) \tag{15}$$

for $d = 3$ and with $\boldsymbol{\alpha} \in \mathbb{R}^3$. The extension of the problem in (8) to 3D is as (16), shown at the bottom of the page, where we used $\times$ to signal a matrix-vector multiplication. We note that the material parameters l, m are taken as in 2D and, thus, may have to be adjusted to 3D parameters depending on the use case.

2) Experiments: As a proof of concept, we tested the 3D implementation on the simulation of the Lamina setup described in Section IV-H, applying our method directly to the resulting 3D volumes instead of slicing them.

The results show that the reconstructions in 3D can also recover well the distribution of stiffness (Figure 15). We stopped the indirect method early because of time constraints (Table IV). In the 3D case, the Mixed-PDE approach

$$\begin{bmatrix} l\varepsilon_{11} + (l-m)(\varepsilon_{22}+\varepsilon_{33}) & m\varepsilon_{12} & m\varepsilon_{13} \\ m\varepsilon_{21} & l\varepsilon_{22} + (l-m)(\varepsilon_{11}+\varepsilon_{33}) & m\varepsilon_{23} \\ m\varepsilon_{31} & m\varepsilon_{32} & l\varepsilon_{33} + (l-m)(\varepsilon_{11}+\varepsilon_{22}) \end{bmatrix} \times \begin{bmatrix} \partial_x \ln(E) \\ \partial_y \ln(E) \\ \partial_z \ln(E) \end{bmatrix}$$
$$= -\begin{bmatrix} \partial_x(l\varepsilon_{11} + (l-m)(\varepsilon_{22}+\varepsilon_{33})) + \partial_y(m\varepsilon_{12}) + \partial_z(m\varepsilon_{13}) \\ \partial_x(m\varepsilon_{21}) + \partial_y((l-m)(\varepsilon_{11}+\varepsilon_{33}) + l\varepsilon_{22}) + \partial_z(m\varepsilon_{23}) \\ \partial_x(m\varepsilon_{31}) + \partial_y(m\varepsilon_{32}) + \partial_z((l-m)(\varepsilon_{11}+\varepsilon_{22}) + l\varepsilon_{33}), \end{bmatrix} \tag{16}$$

Authorized licensed use limited to: EPFL LAUSANNE. Downloaded on March 24,2025 at 15:29:48 UTC from IEEE Xplore. Restrictions apply.

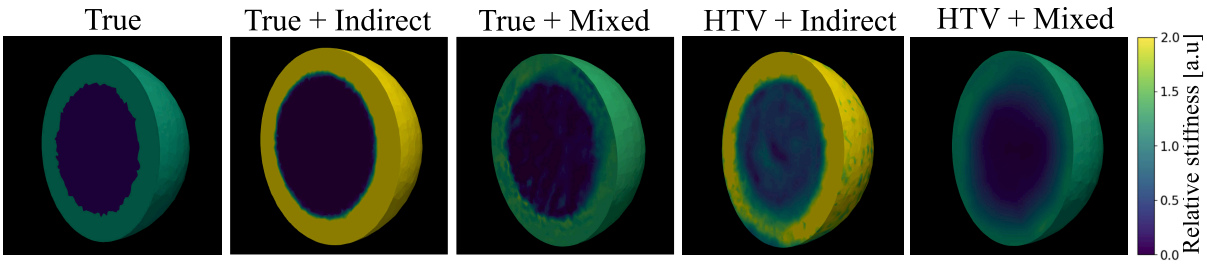

Fig. 15. 3D simulation and its reconstruction from the true displacements ("True") or from warped image volumes using HTV. The indirect method was stopped early. The volumes are of dimension 100 × 100 × 100. We added noise to them (PSNR 30 dB).

is even more relevant because the computation times become very long for the indirect methods (Figure 15). We conclude that our 3D proof of concept is promising, but acknowledge that it requires further testing.

Acknowledgment

The authors would like to thank S. Ghosh and P. Neu for sharing the data on cardiomyocytes. They would also like to thank the anonymous reviewers for their feedback.

References

[1] S. Kwon, W. Yang, D. Moon, and K. S. Kim, "Comparison of cancer cell elasticity by cell type," *J. Cancer*, vol. 11, no. 18, pp. 5403–5412, 2020.
[2] M. Zwerger, C. Y. Ho, and J. Lammerding, "Nuclear mechanics in disease," *Annu. Rev. Biomed. Eng.*, vol. 13, no. 1, pp. 397–428, Aug. 2011.
[3] L. A. Lautscham et al., "Migration in confined 3D environments is determined by a combination of adhesiveness, nuclear volume, contractility, and cell stiffness," *Biophys. J.*, vol. 109, no. 5, pp. 900–913, Sep. 2015.
[4] M. A. Morgan and A. Shilatifard, "Chromatin signatures of cancer," *Genes Develop.*, vol. 29, no. 3, pp. 238–249, Feb. 2015.
[5] G. Felsenfeld, J. Boyes, J. Chung, D. Clark, and V. Studitsky, "Chromatin structure and gene expression," *Proc. Nat. Acad. Sci. USA*, vol. 93, no. 18, pp. 9384–9388, 1996.
[6] A. Groth, W. Rocha, A. Verreault, and G. Almouzni, "Chromatin challenges during DNA replication and repair," *Cell*, vol. 128, no. 4, pp. 721–733, Feb. 2007.
[7] S. M. van der Maarel, D. G. Miller, R. Tawil, G. N. Filippova, and S. J. Tapscott, "Facioscapulohumeral muscular dystrophy: Consequences of chromatin relaxation," *Current Opinion Neurol.*, vol. 25, no. 5, p. 614, 2012.
[8] S. Vidak and R. Foisner, "Molecular insights into the premature aging disease progeria," *Histochem. Cell Biol.*, vol. 145, no. 4, pp. 401–417, Apr. 2016.
[9] S. Dupont and S. A. Wickström, "Mechanical regulation of chromatin and transcription," *Nature Rev. Genet.*, vol. 23, no. 10, pp. 624–643, 2022.
[10] T. Fischer, A. Hayn, and C. T. Mierke, "Effect of nuclear stiffness on cell mechanics and migration of human breast cancer cells," *Frontiers Cell Develop. Biol.*, vol. 8, p. 393, May 2020.
[11] V. Y. Zaitsev et al., "Strain and elasticity imaging in compression optical coherence elastography: The two-decade perspective and recent advances," *J. Biophotonics*, vol. 14, no. 2, Feb. 2021, Art. no. e202000257.
[12] C. M. Hobson, M. R. Falvo, and R. Superfine, "A survey of physical methods for studying nuclear mechanics and mechanobiology," *APL Bioeng.*, vol. 5, no. 4, Dec. 2021, Art. no. 041508.
[13] J. Lammerding, "Mechanics of the nucleus," *Comprehensive Physiol.*, vol. 1, no. 2, p. 783, 2011.
[14] G. Ofek, R. M. Natoli, and K. A. Athanasiou, "In situ mechanical properties of the chondrocyte cytoplasm and nucleus," *J. Biomech.*, vol. 42, no. 7, pp. 873–877, May 2009.
[15] J. Porée, D. Garcia, B. Chayer, J. Ohayon, and G. Cloutier, "Noninvasive vascular elastography with plane strain incompressibility assumption using ultrafast coherent compound plane wave imaging," *IEEE Trans. Med. Imag.*, vol. 34, no. 12, pp. 2618–2631, Dec. 2015.
[16] P. E. Barbone and A. A. Oberai, "Elastic modulus imaging: Some exact solutions of the compressible elastography inverse problem," *Phys. Med. Biol.*, vol. 52, no. 6, pp. 1577–1593, Mar. 2007.
[17] Y. Zhu, T. J. Hall, and J. Jiang, "A finite-element approach for young's modulus reconstruction," *IEEE Trans. Med. Imag.*, vol. 22, no. 7, pp. 890–901, Jul. 2003.
[18] A. A. Oberai, N. H. Gokhale, and G. R. Feijóo, "Solution of inverse problems in elasticity imaging using the adjoint method," *Inverse Problems*, vol. 19, no. 2, pp. 297–313, Apr. 2003.
[19] A. Boquet-Pujadas and J.-C. Olivo-Marin, "Multiple variational image assimilation for accessible micro-elastography," *J. Phys., Conf. Ser.*, vol. 1131, no. 1, 2018, Art. no. 012014.
[20] S. Ghosh, V. C. Cuevas, B. Seelbinder, and C. P. Neu, "Image-based elastography of heterochromatin and euchromatin domains in the deforming cell nucleus," *Small*, vol. 17, no. 5, Feb. 2021, Art. no. 2006109.
[21] P. E. Barbone and N. H. Gokhale, "Elastic modulus imaging: On the uniqueness and nonuniqueness of the elastography inverse problem in two dimensions," *Inverse Problems*, vol. 20, no. 1, pp. 283–296, Feb. 2004.
[22] Y. Kesenci, A. Boquet-Pujadas, M. Unser, and J.-C. Olivo-Marin, "Probing intracellular elasticity with minimal-hessian registration," in *Proc. IEEE 20th Int. Symp. Biomed. Imag. (ISBI)*, Apr. 2023, pp. 1–5.
[23] H. Liu et al., "In situ mechanical characterization of the cell nucleus by atomic force microscopy," *ACS Nano*, vol. 8, no. 4, pp. 3821–3828, Apr. 2014.
[24] A. Vaziri and M. R. K. Mofrad, "Mechanics and deformation of the nucleus in micropipette aspiration experiment," *J. Biomech.*, vol. 40, no. 9, pp. 2053–2062, 2007.
[25] C. J. Bustamante, Y. R. Chemla, S. Liu, and M. D. Wang, "Optical tweezers in single-molecule biophysics," *Nature Rev. Methods Primers*, vol. 1, no. 1, p. 25, 2021.
[26] F. Guilak, "Compression-induced changes in the shape and volume of the chondrocyte nucleus," *J. Biomech.*, vol. 28, no. 12, pp. 1529–1541, Dec. 1995.
[27] C. Gosse and V. Croquette, "Magnetic tweezers: Micromanipulation and force measurement at the molecular level," *Biophys. J.*, vol. 82, no. 6, pp. 3314–3329, Jun. 2002.
[28] Y. Xia, C. R. Pfeifer, and D. E. Discher, "Nuclear mechanics during and after constricted migration," *Acta Mechanica Sinica*, vol. 35, no. 2, pp. 299–308, Apr. 2019.
[29] A. C. Rowat et al., "Nuclear envelope composition determines the ability of neutrophil-type cells to passage through micron-scale constrictions," *J. Biol. Chem.*, vol. 288, no. 12, pp. 8610–8618, Mar. 2013.
[30] D. R. Gossett et al., "Hydrodynamic stretching of single cells for large population mechanical phenotyping," in *Proc. Nat. Acad. Sci. USA*, 2012, vol. 109, no. 20, pp. 7630–7635.
[31] D.-H. Kim, B. Li, F. Si, J. M. Phillip, D. Wirtz, and S. X. Sun, "Volume regulation and shape bifurcation in the cell nucleus," *J. Cell Sci.*, vol. 128, no. 18, pp. 3375–3385, 2015.
[32] R. Prevedel, A. Diz-Muñoz, G. Ruocco, and G. Antonacci, "Brillouin microscopy: An emerging tool for mechanobiology," *Nature Methods*, vol. 16, no. 10, pp. 969–977, Oct. 2019.
[33] P.-J. Wu et al., "Water content, not stiffness, dominates Brillouin spectroscopy measurements in hydrated materials," *Nature Methods*, vol. 15, no. 8, pp. 561–562, Aug. 2018.
[34] D. Wirtz, "Particle-tracking microrheology of living cells: Principles and applications," *Annu. Rev. Biophys.*, vol. 38, no. 1, pp. 301–326, Jun. 2009.

Authorized licensed use limited to: EPFL LAUSANNE. Downloaded on March 24,2025 at 15:29:48 UTC from IEEE Xplore. Restrictions apply.

[35] F. Guilak, J. R. Tedrow, and R. Burgkart, "Viscoelastic properties of the cell nucleus," *Biochem. Biophys. Res. Commun.*, vol. 269, no. 3, pp. 781–786, Mar. 2000.
[36] C. M. Hobson and A. D. Stephens, "Modeling of cell nuclear mechanics: Classes, components, and applications," *Cells*, vol. 9, no. 7, p. 1623, Jul. 2020.
[37] K. T. Sapra et al., "Nonlinear mechanics of lamin filaments and the meshwork topology build an emergent nuclear lamina," *Nature Commun.*, vol. 11, no. 1, p. 6205, Dec. 2020.
[38] L. M. Almassalha et al., "The global relationship between chromatin physical topology, fractal structure, and gene expression," *Sci. Rep.*, vol. 7, no. 1, p. 41061, Jan. 2017.
[39] J. E. Marsden and T. J. Hughes, *Mathematical Foundations of Elasticity*. North Chelmsford, MA, USA: Courier Corporation, 1994.
[40] B. K. P. Horn and B. G. Schunck, "Determining optical flow," *Artif. Intell.*, vol. 17, nos. 1–3, pp. 185–203, Aug. 1981.
[41] D. K. Vig, A. E. Hamby, and C. W. Wolgemuth, "On the quantification of cellular velocity fields," *Biophys. J.*, vol. 110, no. 7, pp. 1469–1475, Apr. 2016.
[42] A. Boquet-Pujadas, J.-C. Olivo-Marin, and N. Guillén, "Bioimage analysis and cell motility," *Patterns*, vol. 2, no. 1, Jan. 2021, Art. no. 100170.
[43] J. Revaud, P. Weinzaepfel, Z. Harchaoui, and C. Schmid, "EpicFlow: Edge-preserving interpolation of correspondences for optical flow," in *Proc. IEEE Conf. Comput. Vis. Pattern Recognit. (CVPR)*, Jun. 2015, pp. 1164–1172.
[44] M. A. Mohamed, H. A. Rashwan, B. Mertsching, M. A. Garcia, and D. Puig, "Illumination-robust optical flow using a local directional pattern," *IEEE Trans. Circuits Syst. Video Technol.*, vol. 24, no. 9, pp. 1499–1508, Sep. 2014.
[45] E. M. Kalmoun, "A new tikhonov-tv regularization for optical flow computation," *Proc. SPIE*, vol. 11373, pp. 644–648, Jan. 2019.
[46] M. J. Black and P. Anandan, "A framework for the robust estimation of optical flow," in *Proc. 4th Int. Conf. Comput. Vis.*, May 1993, pp. 231–236.
[47] D. Sun, C. Liu, and H. Pfister, "Local layering for joint motion estimation and occlusion detection," in *Proc. IEEE Conf. Comput. Vis. Pattern Recognit.*, Jun. 2014, pp. 1098–1105.
[48] Z. Tu et al., "A survey of variational and CNN-based optical flow techniques," *Signal Process., Image Commun.*, vol. 72, pp. 9–24, Mar. 2019.
[49] D. Chen, H. Sheng, Y. Chen, and D. Xue, "Fractional-order variational optical flow model for motion estimation," *Phil. Trans. Roy. Soc. A, Math., Phys. Eng. Sci.*, vol. 371, no. 1990, May 2013, Art. no. 20120148.
[50] A. Chambolle, V. Caselles, D. Cremers, M. Novaga, and T. Pock, "An introduction to total variation for image analysis," *Theor. Found. Numer. Methods Sparse Recovery*, vol. 9, nos. 263–340, p. 227, 2010.
[51] M. Nikolova, "Local strong homogeneity of a regularized estimator," *SIAM J. Appl. Math.*, vol. 61, no. 2, pp. 633–658, Jan. 2000.
[52] R. Ranftl, K. Bredies, and T. Pock, "Non-local total generalized variation for optical flow estimation," in *Proc. 13th Eur. Conf. Comput. Vis.*, Zurich, Switzerland. Cham, Switzerland: Springer, 2014, pp. 439–454.
[53] P. Weinzaepfel, J. Revaud, Z. Harchaoui, and C. Schmid, "DeepFlow: Large displacement optical flow with deep matching," in *Proc. IEEE Int. Conf. Comput. Vis. (ICCV)*, Dec. 2013, pp. 1385–1392.
[54] P. E. Barbone and J. C. Bamber, "Quantitative elasticity imaging: What can and cannot be inferred from strain images," *Phys. Med. Biol.*, vol. 47, no. 12, pp. 2147–2164, Jun. 2002.
[55] X. Pan, K. Liu, J. Bai, and J. Luo, "A regularization-free elasticity reconstruction method for ultrasound elastography with freehand scan," *Biomed. Eng. OnLine*, vol. 13, no. 1, pp. 1–17, Dec. 2014.
[56] A. Boquet-Pujadas and J.-C. Olivo-Marin, "Reformulating optical flow to solve image-based inverse problems and quantify uncertainty," *IEEE Trans. Pattern Anal. Mach. Intell.*, vol. 45, no. 5, pp. 6125–6141, May 2023.
[57] A. Boquet-Pujadas et al., "4D live imaging and computational modeling of a functional gut-on-a-chip evaluate how peristalsis facilitates enteric pathogen invasion," *Sci. Adv.*, vol. 8, no. 42, Oct. 2022, Art. no. eabo5767.
[58] L. T. Biegler, O. Ghattas, M. Heinkenschloss, and B. van Bloemen Waanders, *Large-Scale PDE-Constrained Optimization: An Introduction*. Cham, Switzerland: Springer, 2003.
[59] S. Aziznejad, J. Campos, and M. Unser, "Measuring complexity of learning schemes using Hessian–Schatten total variation," *SIAM J. Math. Data Sci.*, vol. 5, no. 2, pp. 422–445, Jun. 2023.
[60] S. Friedland and L.-H. Lim, "Nuclear norm of higher-order tensors," *Math. Comput.*, vol. 87, no. 311, pp. 1255–1281, Sep. 2017.
[61] L. Qi and S. Hu, "Spectral norm and nuclear norm of a third order tensor," 2019, *arXiv:1909.01529*.
[62] L. Ambrosio, S. Aziznejad, C. Brena, and M. Unser, "Linear inverse problems with Hessian–Schatten total variation," *Calculus Variat. Partial Differ. Equ.*, vol. 63, no. 1, p. 9, Jan. 2024.
[63] L. Ambrosio, C. Brena, and S. Conti, "Functions with bounded Hessian–Schatten variation: Density, variational, and extremality properties," *Arch. Rational Mech. Anal.*, vol. 247, no. 6, p. 111, Dec. 2023.
[64] T. Brox and J. Malik, "Large displacement optical flow: Descriptor matching in variational motion estimation," *IEEE Trans. Pattern Anal. Mach. Intell.*, vol. 33, no. 3, pp. 500–513, Mar. 2011.
[65] S. Lefkimmiatis, J. P. Ward, and M. Unser, "Hessian schatten-norm regularization for linear inverse problems," *IEEE Trans. Image Process.*, vol. 22, no. 5, pp. 1873–1888, May 2013.
[66] A. Beck and M. Teboulle, "Fast gradient-based algorithms for constrained total variation image denoising and deblurring problems," *IEEE Trans. Image Process.*, vol. 18, no. 11, pp. 2419–2434, Nov. 2009.
[67] C. Sumi, A. Suzuki, and K. Nakayama, "Estimation of shear modulus distribution in soft tissue from strain distribution," *IEEE Trans. Biomed. Eng.*, vol. 42, no. 2, pp. 193–202, Feb. 1995.
[68] A. R. Skovoroda, S. Y. Emelianov, and M. O'Donnell, "Tissue elasticity reconstruction based on ultrasonic displacement and strain images," *IEEE Trans. Ultrason., Ferroelectr., Freq. Control*, vol. 42, no. 4, pp. 747–765, Jul. 1995.
[69] A. R. Skovoroda, L. A. Lubinski, S. Y. Emelianov, and M. O'Donnell, "Reconstructive elasticity imaging for large deformations," *IEEE Trans. Ultrason., Ferroelectr., Freq. Control*, vol. 46, no. 3, pp. 523–535, May 1999.
[70] P. G. Ciarlet, *The Finite Element Method for Elliptic Problems*. Philadelphias, PA, USA: SIAM, 2002.
[71] H. A. Van der Vorst, *Iterative Krylov Methods for Large Linear Systems*. Cambridge, U.K.: Cambridge Univ. Press, 2003.
[72] K. B. Nakshatrala, A. Masud, and K. D. Hjelmstad, "On finite element formulations for nearly incompressible linear elasticity," *Comput. Mech.*, vol. 41, no. 4, pp. 547–561, Dec. 2007.
[73] C. M. Hobson, M. Kern, E. T. O'Brien, A. D. Stephens, M. R. Falvo, and R. Superfine, "Correlating nuclear morphology and external force with combined atomic force microscopy and light sheet imaging separates roles of chromatin and lamin A/C in nuclear mechanics," *Mol. Biol. Cell*, vol. 31, no. 16, pp. 1788–1801, Jul. 2020.
[74] W. R. Trickey, F. P. T. Baaijens, T. A. Laursen, L. G. Alexopoulos, and F. Guilak, "Determination of the Poisson's ratio of the cell: Recovery properties of chondrocytes after release from complete micropipette aspiration," *J. Biomech.*, vol. 39, no. 1, pp. 78–87, Jan. 2006.
[75] J. S. Pérez, E. Meinhardt-Llopis, and G. Facciolo, "TV-L1 optical flow estimation," *Image Process. Line*, vol. 3, pp. 137–150, Jul. 2013.
[76] A. Plyer, G. Le Besnerais, and F. Champagnat, "Massively parallel Lucas Kanade optical flow for real-time video processing applications," *J. Real-Time Image Process.*, vol. 11, no. 4, pp. 713–730, Apr. 2016.
[77] B. Seelbinder et al., "Nuclear deformation guides chromatin reorganization in cardiac development and disease," *Nature Biomed. Eng.*, vol. 5, no. 12, pp. 1500–1516, Dec. 2021.
[78] S. Ghosh et al., "Deformation microscopy for dynamic intracellular and intranuclear mapping of mechanics with high spatiotemporal resolution," *Cell Rep.*, vol. 27, no. 5, pp. 1607–1620, Apr. 2019.
[79] E. Nelsen. et al., "Combined atomic force microscope and volumetric light sheet system for correlative force and fluorescence mechanobiology studies," *Sci Rep.*, vol. 10, no. 5, p. 8133, May 2020.
[80] A. Boquet-Pujadas, J. Hardouïn, J. Wen, J. Ignés-Mullol, and F. Sagués, "Inverse measurements in active nematics," 2023, *arXiv:2312.15553*.
[81] J. Steinwachs et al., "Three-dimensional force microscopy of cells in biopolymer networks," *Nature Methods*, vol. 13, no. 2, pp. 171–176, Feb. 2016.
[82] L. Bao, K. Chen, D. Kong, S. Ying, and T. Zeng, "Time multiscale regularization for nonlinear image registration," *Computerized Med. Imag. Graph.*, vol. 112, Mar. 2024, Art. no. 102331.

Authorized licensed use limited to: EPFL LAUSANNE. Downloaded on March 24,2025 at 15:29:48 UTC from IEEE Xplore. Restrictions apply.